

# Simulations of Supernova Remnants in Diffuse Media III. The Population of Buoyant Remnants Above the Milky Way's Disk

R. L. Shelton<sup>1</sup>

*Department of Physics and Astronomy, the University of Georgia, Athens, GA 30602*

`rls@hal.physast.uga.edu`

## ABSTRACT

We model SNRs at a variety of heights above the disk with a detailed numerical simulation that includes non-equilibrium ionization and recombination and follows the remnants' evolution until their hot bubbles have cooled. We analytically calculate the bubbles' buoyant acceleration and frictional drag. From the simulation results, combined with the rates for isolated supernova explosions above a height of 130 pc, we estimate the time and space average  $O^{+5}$ ,  $N^{+4}$ , and  $C^{+3}$  column densities and emission intensities, 1/4 keV soft X-ray surface brightness, area coverage, and volume occupation due to the population of isolated SNRs above the Galaxy's HI layer. Irrespective of assumed supernova explosion energy, ambient nonthermal pressure, or frictional drag coefficient used in the calculations, the predicted  $O^{+5}$  column density as a function of height matches the observed distribution between 130 pc and 2000 pc. The O VI resonance line emission (1032, 1038  $\lambda\lambda$ ) contributes significantly to the average observed intensity. Assuming our modest supernova explosion rate, the population of isolated extraplanar SNRs can explain 80% of the observed 1/4 keV surface brightness attributed to the extraplanar gas beyond the H I layer in the southern hemisphere. Within the range of uncertainty in the SN rate, such SNRs can explain all of this observed emission (400 counts  $s^{-1}$  arcmin<sup>-2</sup>). Thus, extraplanar SNRs could be the most important sources of hot gas between the Local Bubble and  $z \sim 2000$  pc in the relatively quiescent southern hemisphere. These results stand whether the remnants are assumed to be buoyant or not. The population of old extraplanar SNRs should cover most, but not all of the high latitude sky, thus explaining the mottled appearance of the soft X-ray maps (outside of superbubbles). Bright

young extraplanar SNRs should cover less than 1% of the high latitude sky. Perhaps the  $\ell = 247^\circ, b = -64^\circ$  crescent in the 1/4 keV X-ray maps could be such a remnant.

*Subject headings:* hydrodynamics – Galaxy:general – ISM:general – ISM:supernova remnants ultraviolet:ISM – ultraviolet:ISM

## 1. Introduction

About half of the progenitor stars at the Sun’s Galactocentric radius reside above the Galactic H I disk (Ferrière 1998). After they explode, their remnant bubbles will evolve in a relatively rarefied, dust-poor environment. They will expand to greater sizes, have lower interior pressures, lower luminosities, lose less energy via emission by dust grains, and live longer than disk remnants (Cioffi 1991). At any given time, most of the supernova remnants (SNRs) above the H I layer should be dynamically old, having transitioned from the adiabatic to the radiative phase in the first few percent of their lifetimes. Old remnants should contribute to the  $O^{+5}$  and soft X-ray backgrounds even though they are dim (Shelton (1998, 1999), hereafter Papers I and II). The young remnants should be much brighter and so easier to recognize. Known examples of comparatively young extraplanar supernova remnants include SN1006 at  $z \sim 450$  pc (Laming et al. 1996) and the Lupus Loop at  $z \sim 330$  pc (Leahy et al. 1991). In addition, bright arcs in the *ROSAT* 1/4 keV maps at  $l = 247, b = -64$  and  $l = 215, b = -68$  may also be extraplanar SNRs.

The plentitude of isolated SNRs above the Galactic H I layer raises the possibility that they play important roles in heating and ionizing the extraplanar interstellar medium (ISM) and whets our appetite for more information. Considering that SNRs evolving in low density environments can be longlived, might they cover a large solid angle on the high latitude sky or fill a large fraction of the volume of space? Might they create many of the observed high latitude high-stage ions ( $O^{+5}$ ,  $N^{+4}$ , and  $C^{+3}$ ) and soft X-rays? Considering that young SNRs are both bright in soft X-rays and rich in  $O^{+5}$  ions, do soft X-rays and  $O^{+5}$  ions track each other in general, or only in recently shocked gas? How buoyant is the hot gas within SNRs?

Much progress has been made toward understanding these SNRs. According to Cioffi (1991)’s and Paper I’s rough estimates, SNRs fill a small fraction of the extraplanar volume, but cover a large fraction of the high latitude sky. <sup>1</sup> Paper I’s preliminary estimate for the

---

<sup>1</sup>This paradox is possible when a large number of SNRs exist at any given time and each is small on the scale of the available space (fractional area coverage goes as  $N(R/L)^2$ , but fractional volume occupation

number of  $O^{+5}$  ions produced by the population of isolated, extraplanar SNRs accounted for the extraplanar  $O^{+5}$  observed by *Copernicus* (Jenkins 1978a) and the supernova explosion scaleheight (300 pc) matched the observationally determined  $O^{+5}$  scaleheight (Jenkins 1978b). Subsequently, *FUSE* observed a much larger sample of high  $z$  stars and found more  $O^{+5}$  above 300 pc. These new observations suggest that modeling the vertical distribution of SN explosions may be important. *FUSE* also found  $O^{+5}$  moving away from the Galactic plane at more than 100 km sec<sup>-1</sup> (Wakker et al. 2003). This suggests that buoyancy may be important. Another possible sign of buoyant motion in the interstellar medium is an H I “mushroom-shaped cloud”, whose cap may be the squashed shell of a buoyant SNR and whose stem may consist of trailing material (English, et al. 2000). Multidimensional simulations have been able to reproduce mushroom shapes and buoyant acceleration (Jones 1973; Avillez & Mac Low 2001). Could buoyancy explain the large  $O^{+5}$  column densities and scale height?

If we could envision a map of the sky based on the  $O^{+5}$  column density in extraplanar SNRs, it would not look like a similarly constructed map of  $O^{+5}$  resonance line emission, or, for that matter, like a similarly constructed map of soft X-ray emission. The  $O^{+5}$  ions would be more smoothly distributed and cover greater area than the detectable emission. The reason is that SNRs harbor rich stores of high-stage ions throughout their lives, but are bright emitters only during their early stages when the dense, recently shocked gas behind their shockfronts is hot (Slavin & Cox 1992; Cioffi 1991; Shelton 1998, 1999). Probably other types of hot gas structures behave similarly. This difference may explain the difficulty in matching the *FUSE*  $O^{+5}$  column density map (Savage et al. 2003) with the *ROSAT* 1/4 keV map (Snowden et al. 1997). Furthermore, extraplanar SNRs are better emitters of 1/4 keV photons than 3/4 keV photons. Thus, the more smoothly distributed 3/4 keV emission (McCammon et al. 1983; Snowden et al. 1997) cannot be attributed to isolated SNRs, even though some or all of the lumpy 1/4 keV emission can (Paper II, Slavin et al. (2000)).

The Paper I and II analyses were preliminary in the sense that they relied on simulations of SNRs born at a single height above the plane and were meant to be followed by a suite of SNR simulations. The Slavin et al. (2000) project used the entire SNR population rather than the population of isolated SNRs above the Milky Way’s thick disk. Furthermore, their simulations did not include ambient magnetic pressure which can compress old SNRs and therefore increase their UV and X-ray luminosities. Consequently, these two studies predicted significantly different time and space average 1/4 keV surface brightnesses. We resolve these difficulties in the present paper.

---

goes as  $N(R/L)^3$ , where  $N$  is the number of objects and  $R/L$  is the object’s radius divided by the length scale of the available space, thus  $R/L < 1$ .)

Here, we aim to estimate the observable effects of the population of extraplanar SNRs by simulating a suite of remnants at various heights above the Galactic plane and various magnetic field strengths and explosion energies, allowing for buoyancy, and by multiplying by the expected rate of isolated supernova explosions above the Galactic disk. The simulation package used to calculate the time evolution of isolated supernova remnants is described in detail in Paper I and described briefly in Subsection 2.1. The analytic calculations used to predict the buoyant acceleration are spelled out in detail in Subsection 2.2. The ambient conditions and progenitor statistics are presented in Subsections 2.3 and 2.4. Due to the interstellar medium’s variation with height above the plane and due to the uncertainty in the explosion energy and ambient non-thermal pressure, we ran a suite of simulations. Their parameters are presented in Subsection 2.5. The resulting area coverage, volume occupation,  $O^{+5}$ ,  $N^{+4}$ ,  $C^{+3}$ , and soft X-ray predictions for each of the simulated SNRs are tabulated in Subsection 3.1. We combined the individual SNR predictions with the buoyancy calculations and convolved with the rate for isolated supernova explosions above the Galactic disk’s H I layer. The resulting estimates of the time and space averaged area coverage, volume occupation, high stage ion content and emission, and 1/4 keV X-ray intensity due to the population of extraplanar SNRs are presented and discussed in Subsections 3.2 - 3.5. In Section 4, we compare the estimates with  $O^{+5}$  and 1/4 keV X-ray observations.  $O^{+5}$  and soft X-ray emission are far less affected by photoionization than are  $C^{+3}$  and  $N^{+4}$ , so are better tests on the model. The column densities from the calculations agree well with the  $O^{+5}$  column densities observed within the first 2000 pc of the Galactic plane. The simulations also explain much of the observed extraplanar 1/4 keV X-ray emission outside of superbubbles and explain its mottled appearance. We summarize the results in Section 5.

## 2. Simulation Method

### 2.1. Computer Simulation Package

The supernova simulations are performed with a Lagrangian mesh hydrocode whose algorithms model shock dynamics, nonequilibrium ionization and recombination, and non-thermal pressure. Previous investigations found that some form of mixing is necessary in order for the remnants’ centers to retain the modest gas densities surmised from X-ray observations of post Sedov phase SNRs such as W44. The hydrocode models thermal conduction, which diffuses entropy within the remnant’s interior and so approximates the required mixing (Cox et al. (1999); Shelton et al. (1999); Shelton, Kuntz & Petre (2004)). Cui & Cox (1992) found that the electrons and ions behind the SNR shock zone come into equilibrium early in the remnant’s evolution, long before radiative cooling becomes important. As a re-

sult, the SNR’s late term evolution (which plays the largest role in calculating the remnant’s  $O^{+5}$  content, area coverage, and volume occupation) is not affected by our approximation of instantaneous electrons and ion equilibration. Cosmic rays affect SNRs by contributing to the pressure behind the shock, while SNRs affect cosmic rays by accelerating them. Cosmic rays affect SNRs by contributing to the pressure behind the shock, while SNRs affect cosmic rays by accelerating them. In a careful analysis of supernova remnant evolution in the presence of cosmic rays and magnetic fields, Ferrière & Zweibel (1991) explored several detailed interactions, but, nonetheless, found that their simulated SNRs with cosmic rays were qualitatively similar to their simulated SNRs without cosmic rays. In our simulation package, we include an isotropic cosmic ray pressure (see Section 2.5), but neglect detailed interactions. Furthermore, we assume that the interstellar medium’s gas phase metal abundances are approximately solar and so adopt the abundances of Grevesse & Anders (1989). The code is similar to Slavin & Cox (1992, 1993)’s code. Papers I and II used this code, describe it in detail, and present sample simulations. Because the hydrocode’s Lagrangian mesh architecture does not model a stratified ambient media, we combine the SNR simulations with the following analytic buoyancy calculations in order to determine if and how rapidly the remnants rise in the Galaxy’s stratified interstellar medium.

## 2.2. Buoyancy

As a whole, a SNR is not buoyant, because its average density approximately equals that of the surrounding gas. Only the very hot, rarefied interior should be buoyant. Furthermore, buoyancy is probably not relevant for very young remnants because the buoyant acceleration acting on the bubble interiors is outpaced by the remnants’ expansion and because their magnetic fields tie the most buoyant material in their centers to the non-buoyant dense, ionized, postshock gas. Later in a remnant’s evolution, a cool shell develops between its hot bubble interior and its shockfront (see Slavin & Cox (1992), or Paper I for detailed simulations). At this time, buoyant motion may exceed the hot bubble’s expansion and the postshock shell cools, becomes somewhat neutral, and dissipates. It is in this stage that we consider the buoyant force. Because we do not know how well the shell constrains the hot interior nor the strength of frictional drag, we consider a range of cases. In the first, we assume that the SNRs do not rise buoyantly. In the second, we assume that after the cool shell develops, the hot remnant interiors dissociate from the shell and rise buoyantly, but encounter some resistance. In the third, we assume that after the cool shell develops, the hot remnant interiors dissociate from the shell and rise buoyantly, without resistance. Below, we describe our analytical calculations for the buoyant motion of a hot bubble interior encountering frictional drag.

The elementary equation for the acceleration due to buoyancy is:

$$a(z) = g(z)\left(1 - \frac{\rho_a(z)}{\rho_b(z)}\right), \quad (1)$$

where  $g$  is the acceleration of gravity,  $\rho_a$  is the mass density of the ambient medium,  $\rho_b$  is the mass density within the bubble, and  $z$  is the height above the Galactic plane. The acceleration of gravity at the Sun’s galactocentric radius is given by Benjamin & Danly (1997) and Wolfire et al. (1995) as:

$$g(z) = -9.5 \times 10^{-9} \tanh(z/400\text{pc}) \text{ cm s}^{-2}. \quad (2)$$

As the bubble gains speed, it should experience increasing frictional drag. Following Benjamin & Danly (1997), we calculate the frictional acceleration in the direction opposite to motion from

$$a_f = \frac{1}{2}CA_bv_b^2\rho_a/m_b, \quad (3)$$

where  $A_b$  is the cross sectional area of the hot bubble,  $v_b$  is the hot bubble’s velocity relative to the ambient medium  $\rho_a$  is the ambient mass density,  $m_b$  is the mass of the hot bubble (determined from following simulations) and  $C$  is the drag coefficient. If the bubble slides frictionlessly through the ISM, then  $C = 0$ . However, if the bubble sweeps up the overlying ISM, then  $C = 2$ . If, in addition, a low pressure region develops behind the bubble, then  $C$  exceeds 2. The value of  $C$  for hot bubbles in the ISM is poorly known, but simulations suggest (Jones et al. 1996) that it may be around 1. Here we consider 3 cases,  $C = 0$ ,  $C = 1$ , and  $C = \text{large enough to prevent bubble motion}$ .

Generally, the center of the hot bubble is the most rarefied and thus most buoyant, while the periphery of the hot bubble is the densest and least buoyant. A strong buoyancy gradient develops which may allow the interior to rise relative to the periphery. In our calculations of the mass and area of the hot bubble, we include only the buoyant region of the hot bubble. For computational simplicity, we assume that the buoyant region remains intact. Thus, we calculate the force on this region and divide by its mass to find its average acceleration. We then iterate using small time steps to find the velocity and vertical displacement.

As the bubble rises, it passes through successively more rarefied ambient gas. In some cases, a bubble will rise from its birth neighborhood into the overlaying neighborhood. At that point we account for the new environment’s effects on the remnant by switching to the simulation results for a remnant evolving in the new environment. Thus, we use the first part of the simulation for a remnant in the birth neighborhood and the second part of the simulation for a remnant in the overlaying neighborhood. We must deal with the possibility that the two remnants may have differing lifetimes and hence differing maturation rates.

Although the aging process may not be strictly linear, we define a remnant’s “maturity” as the ratio of the present age to the total lifetime, where the remnant’s lifetime is the time required for all of the material in a stationary remnant to cool below  $2 \times 10^4$  K (see Paper I for further discussions of remnant death). When we switch from the remnant evolving in the lower neighborhood to the remnant evolving in the overlaying neighborhood, we match maturities rather than ages. Later in this article, we will perform time integrations. For the integrations, we will not count the time gap between the age of the first remnant and the age of the second. If we were to count that time, we would overestimate the effects of the remnants. Nonetheless, when we allow the remnants to be buoyant, they live longer than stationary remnants, as shown in Figure 1.

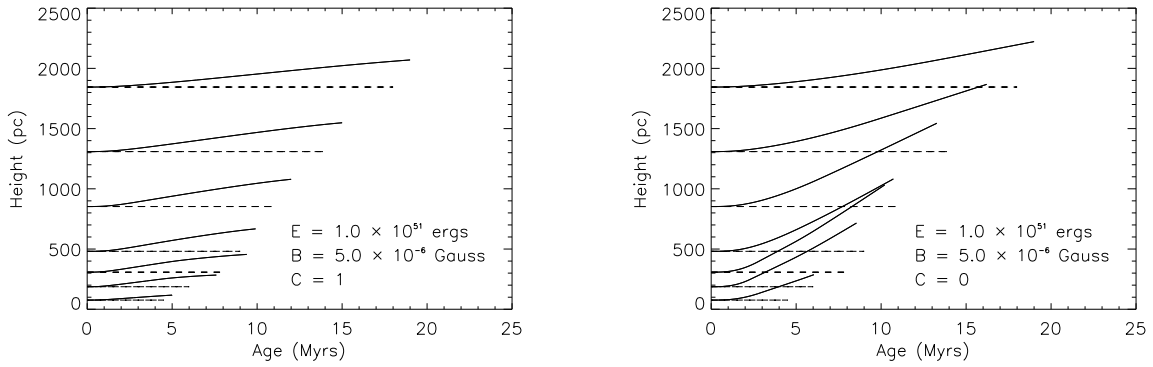


Fig. 1.— In each figure, the dashed lines track the non-buoyant SNRs and the solid lines track the buoyant SNRs as they rise. In the left and right figures, respectively, the drag coefficient,  $C$ , which is used to predict the trajectories of the buoyant SNRs, is set to 1.0 and 0.0, respectively. The height refers to the height of the center of the remnant with respect to the Galactic plane. The height gains for this choice of simulation parameters (explosion energy =  $1.0 \times 10^{51}$  ergs, effective magnetic field strength =  $5.0 \mu\text{G}$ ) lie between those for the other two sets of simulation parameters used in this paper and described in Section 2.5.



### 2.3. The Ambient Medium in the Thick Disk and Lower Halo

Both the hydrocode simulations and the buoyancy calculations require estimates of the ambient density of material. From Ferrière (1998), the vertical distributions of molecular, neutral, warm ionized, and hot hydrogen nuclei are:

$$n_m(z) = 0.58 e^{-(z/81\text{pc})^2} \text{ cm}^{-3} \quad (4)$$

$$n_n(z) = (0.395 e^{-(z/127\text{pc})^2} + 0.107 e^{-(z/318\text{pc})^2} + 0.064 e^{-|z|/403\text{pc}}) \text{ cm}^{-3} \quad (5)$$

$$n_{wi}(z) = (0.0237 e^{-|z|/1 \text{ kpc}} + 0.0013 e^{-|z|/150 \text{ pc}}) \text{ cm}^{-3} \quad (6)$$

$$n_h(z) = 4.8 \times 10^{-4} e^{-|z|/1.5\text{kpc}} \text{ cm}^{-3}. \quad (7)$$

The ratio of helium to hydrogen atoms is approximately 1 to 10, so the total density of atoms is assumed to be approximately 1.1 times the density of hydrogen atoms. From Equations 4 through 7 we see that the H I scaleheight is approximately 130 pc, half of the molecular, atomic, and ionized material lies below  $z \sim 90$  pc, and 80% of the material lies below the scaleheight for isolated supernovae ( $\sim 300$  pc, presented below).

### 2.4. The Distribution of Isolated Supernova Progenitors

From Ferrière (1998), the volumetric rate of Type 1a supernova explosions near the Sun’s Galactocentric radius is:

$$\text{Rate}_{\text{Ia}}(z) = 4.0 \times 10^{-6} e^{-|z|/325\text{pc}} \text{ kpc}^{-3} \text{ yr}^{-1}. \quad (8)$$

The expected rate of isolated Type Ib plus Type II supernova explosions is bracketed by estimates taken from Ferrière (1998) (lower range) and calculated from McKee & Williams (1997) (upper range):

$$\text{Rate}_{\text{Ib+II}}(z) = 1.4 \text{ to } 2.8 \times 10^{-5} e^{-|z|/266\text{pc}} \text{ kpc}^{-3} \text{ yr}^{-1}. \quad (9)$$

Note that isolated explosions account for only 40% of the TypeIb and Type II rate. The remaining explosions occur in clusters near the Galactic midplane. They create superbubbles, which are well analyzed in Ferrière (1998), but outside our frame of interest. For the following calculations, we will use the total isolated SN explosion rate at the Sun’s Galactocentric radius, in which the isolated Type Ib plus Type II rate is taken as the average of the Ferrière (1998) and McKee & Williams (1997) estimates:

$$\text{Rate}_{\text{SN}}(z) = (4.0 \times 10^{-6} e^{-|z|/325\text{pc}} + 2.1 \times 10^{-5} e^{-|z|/266\text{pc}}) \text{ kpc}^{-3} \text{ yr}^{-1}. \quad (10)$$

In more conceptual terms, every million years 2 to 3 isolated progenitor stars explode within an open-ended column beginning at  $z = 130$  pc, extending to  $z = \infty$ , having a cross sectional area of  $1 \text{ kpc}^2$ , and residing at the Sun’s Galactocentric radius.

## 2.5. The SNR Simulation Parameters

A remnant born at the SN progenitor scale height will be surrounded by a medium of density,  $n_o$ , equal to  $0.1 \text{ atoms cm}^{-3}$ . Remnants born at half the scale height will be surrounded by  $\sim 0.3 \text{ atoms cm}^{-3}$  gas while remnants born at twice the scale height will encounter  $\sim 0.03 \text{ atoms cm}^{-3}$  gas. In order to account for the variation in ambient density above the Galactic disk, we performed simulations for the following sample of seven ambient densities:  $0.5 \text{ atoms cm}^{-3}$  (corresponding to a height of  $z_1 = 76 \text{ pc}$ ),  $0.2$  (corresponding to a height of  $z_2 = 190 \text{ pc}$ ),  $0.1$  (corresponding to a height of  $z_3 = 310 \text{ pc}$ ),  $0.05$  (corresponding to a height of  $z_4 = 480 \text{ pc}$ ),  $0.02$  (corresponding to a height of  $z_5 = 850 \text{ pc}$ ),  $0.01$  (corresponding to a height of  $z_6 = 1300 \text{ pc}$ ), and  $0.005 \text{ atoms cm}^{-3}$  (corresponding to a height of  $z_7 = 1800 \text{ pc}$ ).  $z_7$  is roughly 6 times the scaleheight for isolated supernova explosions. The  $n = 0.5 \text{ atoms cm}^{-3}$  simulations were performed for comparison with the others; they will not be included in the extra-planar population. Due to uncertainties in the values of the typical explosion energy, we performed simulations for both  $E_o = 0.5 \times 10^{51} \text{ ergs}$  and  $E_o = 1.0 \times 10^{51} \text{ ergs}$  which represent the typical range of estimated explosion energies. At any given height, we have approximated the SNRs' environment as being homogeneous with a temperature,  $T$ , of  $1.0 \times 10^4 \text{ K}$ . At this temperature, the hydrogen in this gas is ionized, as is typical of the Reynolds layer and of the plasma surrounding and pre-ionized by supernova remnants. The turbulent pressure is thought to be small and is not explicitly included in the hydrocode simulations. The magnetic and cosmic ray pressures are swept into a single term called the nonthermal pressure,  $P_{nt}$ . Observational and theoretical estimates of their values in the thick disk are sparse, with the values chosen for the simulations,  $P_{nt} = 1800$  and  $7200 \text{ K cm}^{-3}$ , being well within the probable range. If  $B_{eff}$  is the effective magnetic field strength, where  $P_{nt} = B_{eff}^2 / (8\pi)$ , then the chosen nonthermal pressures correlate to  $B_{eff} = 2.5$  and  $5.0 \mu\text{G}$ . We set  $B_{eff} = 2.5 \mu\text{G}$  only when also setting  $E_o = 0.5 \times 10^{51} \text{ ergs}$ . Thus for every choice of ambient density in our sample, we have performed three simulations, the first having  $E_o = 0.5 \times 10^{51} \text{ ergs}$  and  $B_{eff} = 2.5 \mu\text{G}$ , the second having  $E_o = 0.5 \times 10^{51} \text{ ergs}$  and  $B_{eff} = 5.0 \mu\text{G}$ , and the third having  $E_o = 1.0 \times 10^{51} \text{ ergs}$  and  $B_{eff} = 5.0 \mu\text{G}$ . In all, we report on 21 simulations. Their parameters are listed in Table 1.

Table 1. Parameters for SNR Simulations

$z$ (pc)	$n_o$ (atoms cm <sup>-3</sup> )	$E_o$ (10 <sup>51</sup> ergs)	$B_{eff}$ ( $\mu$ G)	Name
76	0.5	0.5	2.5	halo 65
”	”	”	5.0	halo 62
”	”	1.0	”	halo 64
190	0.2	0.5	2.5	halo 59
”	”	”	5.0	halo 57
”	”	1.0	”	halo 58
310	0.1	0.5	2.5	halo 92
”	”	”	5.0	halo 91
”	”	1.0	”	halo 90
480	0.05	0.5	2.5	halo 110
”	”	”	5.0	halo 111
”	”	1.0	”	halo 109
850	0.02	0.5	2.5	halo 100
”	”	”	5.0	halo 101
”	”	1.0	”	halo 99
1300	0.01	0.5	2.5	halo 103
”	”	”	5.0	halo 104
”	”	1.0	”	halo 102
1800	0.005	0.5	2.5	halo 106
”	”	”	5.0	halo 107
”	”	1.0	”	halo 105

### 3. Simulation Results

#### 3.1. Individual Isolated Remnants

Each computer simulation yielded detailed, comprehensive predictions of the remnant’s physical state as a function of time. The temperature, pressure, velocity, high ion content, high ion absorption line profile, X-ray spectrum, and X-ray luminosity of a sample remnant as a function of time are presented in Papers I and II. In the present paper, we are focusing on the bulk physical and observable effects of the population of isolated extraplanar SNRs and so we will extract a complementary set of information from each simulation.

First, we turn our attention to the cross sectional area covered by supernova remnants. When we look up into the Earth’s atmosphere we see that some fraction of the sky is covered by the population of clouds. Similarly, we can imagine that some fraction of the Galactic high latitude sky is covered by the population of supernova remnants. Determining what this fraction is will help us to interpret high latitude observations of hot gas. Theoretically, the fraction of sky covered by SNRs above a height  $\mathcal{Z}$  is  $\int_{\mathcal{Z}}^{\infty} \text{Rate}_{\text{SN}}(z) \times (\int \pi R^2(z, t) dt) dz$ , where  $\text{Rate}_{\text{SN}}$  is given in Equation 10 and  $R(z, t)$  is the radius of a remnant of age  $t$  and evolving at height  $z$ . In this subsection, we determine the second factor,  $\int \pi R^2(z, t) dt$ , the time integrated area of a SNR evolving at height  $z$ . (We will use the integral to calculate the fractional area coverage in the following subsection.) We approximate the integral as  $\sum \pi R^2(z, t) \times \Delta t$ . We use up to 26 time slices for each summation and, unless stated otherwise, we sum through the end of the remnant’s life. The radius is determined from the location of the shock front when the remnant is young and from Paper I’s bubble boundary criterion when the remnant is old enough to have a cool shell. According to this criterion, previously shocked material that has cooled to a temperature less than  $2 \times 10^4$  K is considered to be part of the shell or environmental ISM while hotter material is considered to be part of the hot bubble. The time integrated area of each simulated SNR is presented in Table 2. We added a column listing the integrated area for the remnants’ early stage, the pre-shell formation (PSF) phase, which ends when the gas immediately behind the shockfront is no longer heated to more than  $3 \times 10^4$  K. This column is identified by the “psf” notation in the summation. The pre-shell formation phase is worth attention because during this stage the dense gas behind the shockfront is very hot and hence luminous in soft X-rays and UV photons. As a result, the remnant could probably be observed and identified as a distinct entity during this stage. At the end of this stage, the gas behind the shockfront undergoes rapid radiative cooling and so evolves into a cool shell which separates the ever-expanding shockfront from the hot, rarefied interior. Although the remaining hot interior (the ‘hot bubble’) can be sufficiently hot and ionized to produce soft X-rays and UV photons, its density and therefore its intensity will be less than previously. As a result, an old remnant

might not be observed or identified as a distinct entity. Nonetheless, as we will show later, the vast majority of the ions (in a time integrated calculation) result from the post-shell formation phase. Note that “halo 106” has a larger pre-shell formation area integral than “halo 107” and “halo 108” because its shell formed later.

Let us turn our attention to the volume occupied by SNRs. At any given moment, some regions of the Galaxy are occupied by SNRs while others are not. Ignoring overlap, the average fraction of space at a height of  $z$  which is occupied by SNRs (the “filling fraction”) can be estimated from:  $\text{Rate}_{\text{SN}}(z) \times (\int \frac{4}{3}\pi R^3(z, t) dt)$ . In this subsection, we determine the second factor in the overall integration,  $\int \frac{4}{3}\pi R^3(z, t) dt$ , the time integrated volume. We approximate this integral (which is called the “four-volume” in Slavin & Cox (1993)) as  $\sum \frac{4}{3}\pi R^3(z, t) \Delta t$ . Table 2 presents the time integrated volumes of individual simulated remnants. These values will be used in the following subsection to calculate the filling fraction of SNR gas.

In preparation for calculating the average  $\text{O}^{+5}$ ,  $\text{N}^{+4}$ , and  $\text{C}^{+3}$  column densities in the following subsection, we calculate the time integrated number of ions per SNR here. The integrals are  $\int \int_0^R n_{\text{ion}}(r, t) 4\pi r^2 dr dt$ , where  $n_{\text{ion}}(r, t)$  is the volume density of the chosen ion at the radius  $r$  from the remnant’s center and at a time  $t$ . The integrals are approximated by summations with respect to time and radius and presented in Table 3. Note that  $\text{C}^{+3}$ , and to a lesser extent,  $\text{N}^{+4}$  can be produced via photoionization or collisional ionization. Here, we report on only the collisionally ionized  $\text{C}^{+3}$  and  $\text{N}^{+4}$ . As in Table 2, additional columns are provided for the integrals through the pre-shell-formation (“psf”) stage of evolution.

Similarly, we calculate the energy released in  $\text{O}^{+5}$ ,  $\text{N}^{+4}$ , and  $\text{C}^{+3}$  resonance line doublet photons ( $\text{O}^{+5}$ : 1032, 1038 Å;  $\text{N}^{+4}$ : 1239, 1243 Å;  $\text{C}^{+3}$ : 1548, 1551 Å). The energy released by a single SNR in a particular doublet is approximated as the doublet’s luminosity summed over time,  $\sum L \Delta t$ . See Table 4. We also calculate the energy released in 1/4 keV soft X-ray photons. The time integrated luminosity is approximated as  $\sum L_{1/4 \text{ keV}} \Delta t$ . The soft X-ray photons are scattered across a spectrum. So, in order to compare our predictions with observations and other calculations, we convolve the spectra with the *ROSAT* response functions for the R1 and R2 bands and report the results in units of *ROSAT* R1 + R2 counts  $\text{cm}^{-2}$ . See Table 5. As in the other tables, a column is provided for the contribution from the pre-shell formation phase, when the remnants are young, bright, and most easily identified as individual objects.

Table 2.

Simulated Remnant	$\sum_0^{psf} \pi R^2 \times \Delta t$ (kpc <sup>2</sup> yr)	$\sum \pi R^2 \times \Delta t$ (kpc <sup>2</sup> yr)	$\sum_0^{psf} \frac{4}{3} \pi R^3 \times \Delta t$ (kpc <sup>3</sup> yr)	$\sum \frac{4}{3} \pi R^3 \times \Delta t$ (kpc <sup>3</sup> yr)
<u><math>n_o = 0.5 \text{ cm}^{-3}</math></u>				
halo 65	16	25,000	0.35	1500
halo 62	35	18,000	0.77	980
halo 64	72	29,000	2.2	1900
<u><math>n_o = 0.2 \text{ cm}^{-3}</math></u>				
halo 59	81	61,000	2.7	4700
halo 57	81	31,000	2.7	2100
halo 58	110	58,000	4.2	4800
<u><math>n_o = 0.1 \text{ cm}^{-3}</math></u>				
halo 92	360	110,000	18	10,000
halo 91	220	49,000	10	3800
halo 90	300	91,000	15	8700
<u><math>n_o = 0.05 \text{ cm}^{-3}</math></u>				
halo 110	960	170,000	63	19,000
halo 111	500	75,000	29	6600
halo 109	1300	140,000	100	15,000
<u><math>n_o = 0.02 \text{ cm}^{-3}</math></u>				
halo 100	740	300,000	53	40,000
halo 101	750	140,000	54	15,000
halo 99	1000	260,000	83	34,000
<u><math>n_o = 0.01 \text{ cm}^{-3}</math></u>				
halo 103	1000	480,000	84	72,000
halo 104	1000	250,000	87	31,000
halo 102	1400	460,000	130	69,000
<u><math>n_o = 0.005 \text{ cm}^{-3}</math></u>				
halo 106	6800	800,000	940	140,000
halo 107	1400	500,000	140	73,000
halo 105	1800	900,000	210	160,000



Table 3.

Simulated Remnant	$\sum_0^{psf} \text{O}^{+5} \Delta t$ ( $\text{O}^{+5}$ ion yr)	$\sum \text{O}^{+5} \Delta t$ ( $\text{O}^{+5}$ ion yr)	$\sum_0^{psf} \text{N}^{+4} \Delta t$ ( $\text{N}^{+4}$ ion yr)	$\sum \text{N}^{+4} \Delta t$ ( $\text{N}^{+4}$ ion yr)	$\sum_0^{psf} \text{C}^{+3} \Delta t$ ( $\text{C}^{+3}$ ion yr)	$\sum \text{C}^{+3} \Delta t$ ( $\text{C}^{+3}$ ion yr)
halo 65	$2.7 \times 10^{58}$	$9.2 \times 10^{60}$	$1.8 \times 10^{57}$	$1.0 \times 10^{60}$	$1.4 \times 10^{57}$	$2.4 \times 10^{60}$
halo 62	$2.1 \times 10^{59}$	$8.5 \times 10^{60}$	$1.6 \times 10^{58}$	$9.0 \times 10^{59}$	$6.6 \times 10^{58}$	$1.6 \times 10^{60}$
halo 64	$5.0 \times 10^{59}$	$1.9 \times 10^{61}$	$4.8 \times 10^{58}$	$1.9 \times 10^{60}$	$5.1 \times 10^{58}$	$3.2 \times 10^{60}$
halo 59	$2.7 \times 10^{59}$	$1.9 \times 10^{61}$	$1.1 \times 10^{58}$	$2.2 \times 10^{60}$	$8.6 \times 10^{57}$	$4.6 \times 10^{60}$
halo 57	$3.2 \times 10^{59}$	$2.0 \times 10^{61}$	$1.2 \times 10^{58}$	$1.6 \times 10^{60}$	$1.5 \times 10^{58}$	$2.7 \times 10^{60}$
halo 58	$2.0 \times 10^{59}$	$4.2 \times 10^{61}$	$1.2 \times 10^{58}$	$3.3 \times 10^{60}$	$1.5 \times 10^{58}$	$5.4 \times 10^{60}$
halo 92	$1.6 \times 10^{60}$	$3.4 \times 10^{61}$	$9.9 \times 10^{58}$	$3.8 \times 10^{60}$	$1.6 \times 10^{59}$	$7.5 \times 10^{60}$
halo 91	$6.4 \times 10^{59}$	$3.6 \times 10^{61}$	$6.6 \times 10^{58}$	$2.6 \times 10^{60}$	$6.1 \times 10^{58}$	$4.7 \times 10^{60}$
halo 90	$8.1 \times 10^{59}$	$7.5 \times 10^{61}$	$3.4 \times 10^{58}$	$5.0 \times 10^{60}$	$3.7 \times 10^{58}$	$9.0 \times 10^{60}$
halo 110	$2.8 \times 10^{60}$	$6.4 \times 10^{61}$	$2.9 \times 10^{59}$	$6.7 \times 10^{60}$	$4.7 \times 10^{59}$	$1.3 \times 10^{61}$
halo 111	$1.4 \times 10^{60}$	$6.0 \times 10^{61}$	$8.7 \times 10^{58}$	$4.3 \times 10^{60}$	$2.4 \times 10^{59}$	$8.9 \times 10^{60}$
halo 109	$4.5 \times 10^{60}$	$1.3 \times 10^{62}$	$3.0 \times 10^{59}$	$8.3 \times 10^{60}$	$5.1 \times 10^{59}$	$1.6 \times 10^{61}$
halo 100	$1.3 \times 10^{60}$	$1.4 \times 10^{62}$	$7.7 \times 10^{58}$	$1.4 \times 10^{61}$	$9.8 \times 10^{58}$	$2.8 \times 10^{61}$
halo 101	$1.7 \times 10^{60}$	$1.2 \times 10^{62}$	$1.5 \times 10^{59}$	$8.9 \times 10^{60}$	$1.8 \times 10^{59}$	$2.1 \times 10^{61}$
halo 99	$1.8 \times 10^{60}$	$2.4 \times 10^{62}$	$1.1 \times 10^{59}$	$1.7 \times 10^{61}$	$1.3 \times 10^{59}$	$3.9 \times 10^{61}$
halo 103	$1.3 \times 10^{60}$	$2.4 \times 10^{62}$	$8.1 \times 10^{58}$	$2.3 \times 10^{61}$	$1.2 \times 10^{59}$	$5.2 \times 10^{61}$
halo 104	$1.7 \times 10^{60}$	$1.9 \times 10^{62}$	$1.3 \times 10^{59}$	$1.5 \times 10^{61}$	$1.7 \times 10^{59}$	$3.7 \times 10^{61}$
halo 102	$1.9 \times 10^{60}$	$3.9 \times 10^{62}$	$1.3 \times 10^{59}$	$2.9 \times 10^{61}$	$1.8 \times 10^{59}$	$7.2 \times 10^{61}$
halo 106	$8.3 \times 10^{60}$	$3.9 \times 10^{62}$	$6.7 \times 10^{59}$	$3.7 \times 10^{61}$	$2.8 \times 10^{60}$	$9.4 \times 10^{61}$
halo 107	$2.1 \times 10^{60}$	$3.7 \times 10^{62}$	$1.5 \times 10^{59}$	$3.3 \times 10^{61}$	$2.4 \times 10^{59}$	$8.6 \times 10^{61}$
halo 105	$2.6 \times 10^{60}$	$7.6 \times 10^{62}$	$1.9 \times 10^{59}$	$6.4 \times 10^{61}$	$3.0 \times 10^{59}$	$1.7 \times 10^{62}$



Table 4.

Simulated Remnant	$\sum_0^{psf} L_{O+5} \Delta t$ (ergs)	$\sum L_{O+5} \Delta t$ (ergs)	$\sum_0^{psf} L_{N+4} \Delta t$ (ergs)	$\sum L_{N+4} \Delta t$ (ergs)	$\sum_0^{psf} L_{C+3} \Delta t$ (ergs)	$\sum L_{C+3} \Delta t$ (ergs)
halo 65	$5.6 \times 10^{47}$	$1.0 \times 10^{49}$	$5.4 \times 10^{46}$	$1.8 \times 10^{48}$	$4.6 \times 10^{46}$	$7.4 \times 10^{48}$
halo 62	$3.2 \times 10^{48}$	$1.0 \times 10^{49}$	$2.4 \times 10^{48}$	$7.4 \times 10^{48}$	$2.4 \times 10^{48}$	$7.4 \times 10^{48}$
halo 64	$1.4 \times 10^{49}$	$3.9 \times 10^{49}$	$2.1 \times 10^{48}$	$7.1 \times 10^{48}$	$3.0 \times 10^{48}$	$1.4 \times 10^{49}$
halo 59	$3.3 \times 10^{48}$	$1.4 \times 10^{49}$	$1.6 \times 10^{47}$	$1.8 \times 10^{48}$	$1.3 \times 10^{47}$	$5.0 \times 10^{48}$
halo 57	$3.9 \times 10^{48}$	$1.6 \times 10^{49}$	$1.7 \times 10^{47}$	$1.6 \times 10^{48}$	$2.2 \times 10^{47}$	$4.4 \times 10^{48}$
halo 58	$2.1 \times 10^{48}$	$2.8 \times 10^{49}$	$1.4 \times 10^{47}$	$3.4 \times 10^{48}$	$1.8 \times 10^{47}$	$1.1 \times 10^{49}$
halo 92	$9.4 \times 10^{48}$	$1.6 \times 10^{49}$	$7.6 \times 10^{47}$	$1.9 \times 10^{48}$	$1.1 \times 10^{48}$	$4.6 \times 10^{48}$
halo 91	$3.4 \times 10^{48}$	$1.5 \times 10^{49}$	$5.2 \times 10^{47}$	$2.2 \times 10^{48}$	$5.8 \times 10^{47}$	$4.2 \times 10^{48}$
halo 90	$4.6 \times 10^{48}$	$3.0 \times 10^{49}$	$2.3 \times 10^{47}$	$3.2 \times 10^{48}$	$2.5 \times 10^{47}$	$9.7 \times 10^{48}$
halo 110	$7.6 \times 10^{48}$	$1.4 \times 10^{49}$	$1.1 \times 10^{48}$	$2.2 \times 10^{48}$	$1.6 \times 10^{48}$	$4.2 \times 10^{48}$
halo 111	$3.6 \times 10^{48}$	$1.5 \times 10^{49}$	$2.8 \times 10^{47}$	$1.6 \times 10^{48}$	$9.0 \times 10^{47}$	$4.2 \times 10^{48}$
halo 109	$1.2 \times 10^{49}$	$3.4 \times 10^{49}$	$1.0 \times 10^{48}$	$3.5 \times 10^{48}$	$1.4 \times 10^{48}$	$6.4 \times 10^{48}$
halo 100	$1.2 \times 10^{48}$	$1.2 \times 10^{49}$	$9.1 \times 10^{46}$	$1.6 \times 10^{48}$	$1.3 \times 10^{47}$	$2.7 \times 10^{48}$
halo 101	$1.4 \times 10^{48}$	$1.9 \times 10^{49}$	$1.7 \times 10^{47}$	$2.1 \times 10^{48}$	$2.6 \times 10^{47}$	$3.3 \times 10^{48}$
halo 99	$1.4 \times 10^{48}$	$3.5 \times 10^{49}$	$1.0 \times 10^{47}$	$3.5 \times 10^{48}$	$1.4 \times 10^{47}$	$5.0 \times 10^{48}$
halo 103	$4.0 \times 10^{47}$	$1.2 \times 10^{49}$	$3.1 \times 10^{46}$	$1.6 \times 10^{48}$	$5.7 \times 10^{46}$	$3.0 \times 10^{48}$
halo 104	$5.1 \times 10^{47}$	$2.0 \times 10^{49}$	$5.0 \times 10^{46}$	$1.9 \times 10^{48}$	$8.6 \times 10^{46}$	$3.0 \times 10^{48}$
halo 102	$5.1 \times 10^{47}$	$3.8 \times 10^{49}$	$4.1 \times 10^{46}$	$3.6 \times 10^{48}$	$7.1 \times 10^{46}$	$5.6 \times 10^{48}$
halo 106	$1.1 \times 10^{48}$	$1.5 \times 10^{49}$	$1.3 \times 10^{47}$	$1.9 \times 10^{48}$	$6.3 \times 10^{47}$	$4.6 \times 10^{48}$
halo 107	$2.2 \times 10^{47}$	$2.2 \times 10^{49}$	$2.1 \times 10^{46}$	$2.3 \times 10^{48}$	$4.1 \times 10^{46}$	$4.3 \times 10^{48}$
halo 105	$2.4 \times 10^{47}$	$4.5 \times 10^{49}$	$2.1 \times 10^{46}$	$4.4 \times 10^{48}$	$4.2 \times 10^{46}$	$8.8 \times 10^{48}$

Table 5.

Simulated Remnant	$\sum_0^{psf} L_{1/4 \text{ keV}} \times \Delta t$ (ROSAT R1 + R2 counts cm <sup>2</sup> )	$\sum L_{1/4 \text{ keV}} \times \Delta t$ (ROSAT R1 + R2 counts cm <sup>2</sup> )
halo 65	$6.9 \times 10^{59}$	$2.4 \times 10^{60}$
halo 62	$2.2 \times 10^{60}$	$5.1 \times 10^{60}$
halo 64	$9.9 \times 10^{59}$	$3.1 \times 10^{60}$
halo 59	$8.4 \times 10^{59}$	$1.7 \times 10^{60}$
halo 57	$8.0 \times 10^{59}$	$1.7 \times 10^{60}$
halo 58	$1.4 \times 10^{60}$	$4.0 \times 10^{60}$
halo 92	$9.5 \times 10^{59}$	$1.2 \times 10^{60}$
halo 91	$7.2 \times 10^{59}$	$1.3 \times 10^{60}$
halo 90	$1.3 \times 10^{60}$	$3.0 \times 10^{60}$
halo 110	$7.0 \times 10^{59}$	$9.0 \times 10^{59}$
halo 111	$5.1 \times 10^{59}$	$1.1 \times 10^{60}$
halo 109	$1.3 \times 10^{60}$	$2.5 \times 10^{60}$
halo 100	$2.6 \times 10^{59}$	$7.2 \times 10^{59}$
halo 101	$2.3 \times 10^{59}$	$1.2 \times 10^{60}$
halo 99	$4.1 \times 10^{59}$	$2.9 \times 10^{60}$
halo 103	$1.5 \times 10^{59}$	$5.9 \times 10^{59}$
halo 104	$1.3 \times 10^{59}$	$1.5 \times 10^{60}$
halo 102	$2.3 \times 10^{59}$	$3.5 \times 10^{60}$
halo 106	$2.1 \times 10^{59}$	$5.8 \times 10^{59}$
halo 107	$7.4 \times 10^{58}$	$1.5 \times 10^{60}$
halo 105	$1.2 \times 10^{59}$	$3.7 \times 10^{60}$

### 3.2. SNR Population: Area Coverage and Volume Occupation

In this and the following two subsections, we predict the effects of the population of isolated extra-planar supernova remnants. For example, we will calculate the fraction of the high latitude sky’s area that is covered by supernova remnants residing above a height,  $\mathcal{Z}$ , of 130 pc. The necessary integral, presented in Section 3.1, will be approximated by the summation  $\sum_{\mathcal{Z}}^{\infty} (\text{Rate}_{\text{SN}}(z) \times \sum \pi R^2(z, t) \Delta t)$ . The first step in handling the gradients in ambient density and SN rate with respect to  $z$  is to segment the thick disk and halo into six plane parallel slabs whose boundaries reside at the midpoints between  $z_1, z_2, z_3, z_4, z_5, z_6$ , and  $z_7$ . The top slab extends to  $z = \infty$ . (This parceling scheme begins at  $z = 130$  pc, the scaleheight for the Galactic H I layer, thus excludes the  $z_1, n_o = 0.5 \text{ cm}^{-3}$  simulations which had been created for comparison with the other simulations.)

We then integrate  $\text{Rate}_{\text{SN}}(z)$ , the isolated SN rate per unit volume and time given in Equation 10, from the lower to the upper boundary of each slab. We multiply each slab’s rate integral by the time integrated cross sectional area for a single SNR residing in that slab tabulated in Table 2. This act implicitly treats all SNRs residing within a slab as if they are residing at the representative height of the slab (i.e.  $z_2, z_3$ , etc.). For each of the slabs, Table 6 lists the integrated SN rates and the fraction of area covered by the population of SNRs if the remnants are stationary. Next, we calculate the effects of the entire population of isolated SNRs born above 130 pc. We sum the fractional area coverages of the six slabs. For stationary SNRs, we use the area coverage values listed in Table 6. For buoyant SNRs, we adjust the time integrated cross sectional areas to account for the time spent in the various slabs. The results for both buoyant and non-buoyant SNRs are tabulated in Table 7. Note that we maintain accuracy to several significant digits during all calculations, but round to two significant digits when reporting results.

Table 6 implies that about 1% of the high latitude sky is covered by young, presumably bright and recognizable SNRs (the pre-shell formation remnants). Depending on the assumed simulation parameters and drag coefficient, 30% to 90% of the sky is covered by the hot gas in SNRs of any age<sup>2</sup>. Although the older SNRs that account for most of the area coverage are not as recognizable as their younger cousins, they still harbor large stores of  $\text{O}^{+5}$ ,  $\text{N}^{+4}$ , and  $\text{C}^{+3}$  which are observationally important.

The “filling fraction”, the fraction of volume at a given height that is filled by extraplanar supernova remnants is simply:  $\text{Rate}_{\text{SN}}(z) \times \sum \frac{4}{3} \pi R^3(z, t) \Delta t$ . We calculate the filling fraction

---

<sup>2</sup>The cross section of a SNR residing at a given height may overlap with the cross section of a SNR residing at another height. Therefore the probability that one or more SNR lie along a sightline perpendicular to the Galactic plane is somewhat smaller than the sums presented.

at the representative height of a slab (i.e.  $z_2, z_3, z_4, z_5, z_6,$  or  $z_7$ ) by calculating the SN explosion rate at the chosen height and then multiplying by the time integrated volume occupation of a single SNR born at the chosen height (taken from Table 2). The resulting filling fractions for non-buoyant SNRs are listed in Table 6. At all examined heights, isolated non-buoyant SNR bubbles fill less than 10% of the volume. If the remnants are buoyant, then the filling fractions in the first couple of slabs would be even smaller, while the minute filling fractions in the upper slabs would be somewhat larger. The smallness of our estimates echo those from other studies, such as Ferrière (1998). On account of their small volume occupations, it is very unlikely that hot supernova remnant bubbles will collide with each other. Interestingly, the volume filling fraction reaches its maximum near the SN scaleheight. This is because the SN rate decreases as a function of  $z$ , the remnants' size and longevity increase as a function of  $z$ , and the maximum product occurs around  $z = 300$  pc.

Table 6.

Slab	Height (pc)	$\int$ SN Rate $dz$ (kpc <sup>-2</sup> yr <sup>-1</sup> )	PSF Area Coverage (%)	Total Area Coverage (%)	PSF Volume Filled (%)	Total Volume Filled (%)
$E_o = 0.5 \times 10^{51}$ ergs						
$B_{eff} = 2.5 \mu\text{G}$						
$n = 0.2 \text{ atom cm}^{-3}$	130 to 250	$1.5 \times 10^{-6}$	0.012	8.9	0.0034	6.0
$n = 0.1 \text{ atom cm}^{-3}$	250 to 390	$1.15 \times 10^{-6}$	0.041	12	0.014	7.9
$n = 0.05 \text{ atom cm}^{-3}$	390 to 670	$1.0 \times 10^{-6}$	0.099	18	0.024	7.2
$n = 0.02 \text{ atom cm}^{-3}$	670 to 1100	$4.8 \times 10^{-7}$	0.036	15	0.0062	4.7
$n = 0.01 \text{ atom cm}^{-3}$	1100 to 1600	$1.2 \times 10^{-7}$	0.012	5.6	0.0020	1.7
$n = 0.005 \text{ atom cm}^{-3}$	<u>1600 to <math>\infty</math></u>	<u><math>2.5 \times 10^{-8}</math></u>	<u>0.017</u>	<u>2.0</u>	0.00028	0.041
Sum	130 to $\infty$	$4.3 \times 10^{-6}$	0.22	61		
$E_o = 0.5 \times 10^{51}$ ergs						
$B_{eff} = 5.0 \mu\text{G}$						
$n = 0.2 \text{ atom cm}^{-3}$	130 to 250	$1.5 \times 10^{-6}$	0.012	4.6	0.0034	2.7
$n = 0.1 \text{ atom cm}^{-3}$	250 to 390	$1.2 \times 10^{-6}$	0.026	5.6	0.0078	3.0
$n = 0.05 \text{ atom cm}^{-3}$	390 to 670	$1.0 \times 10^{-6}$	0.051	7.7	0.011	2.5
$n = 0.02 \text{ atom cm}^{-3}$	670 to 1100	$4.8 \times 10^{-7}$	0.036	6.8	0.0063	1.7
$n = 0.01 \text{ atom cm}^{-3}$	1100 to 1600	$1.2 \times 10^{-7}$	0.012	3.0	0.0021	0.73
$n = 0.005 \text{ atom cm}^{-3}$	<u>1600 to <math>\infty</math></u>	<u><math>2.5 \times 10^{-8}</math></u>	<u>0.0035</u>	<u>1.3</u>	$4.2 \times 10^{-5}$	0.022
Sum	130 to $\infty$	$4.3 \times 10^{-6}$	0.14	29		
$E_o = 1.0 \times 10^{51}$ ergs						
$B_{eff} = 5.0 \mu\text{G}$						
$n = 0.2 \text{ atom cm}^{-3}$	130 to 250	$1.5 \times 10^{-6}$	0.016	8.4	0.0053	6.0
$n = 0.1 \text{ atom cm}^{-3}$	250 to 390	$1.2 \times 10^{-6}$	0.034	11	0.012	6.8
$n = 0.05 \text{ atom cm}^{-3}$	390 to 670	$1.0 \times 10^{-6}$	0.14	14	0.038	5.8
$n = 0.02 \text{ atom cm}^{-3}$	670 to 1100	$4.8 \times 10^{-7}$	0.048	12.5	0.0097	3.9
$n = 0.01 \text{ atom cm}^{-3}$	1100 to 1600	$1.2 \times 10^{-7}$	0.016	5.4	0.0031	1.6
$n = 0.005 \text{ atom cm}^{-3}$	<u>1600 to <math>\infty</math></u>	<u><math>2.5 \times 10^{-8}</math></u>	<u>0.0046</u>	<u>2.3</u>	$6.3 \times 10^{-5}$	0.049
Sum	21 to $\infty$	$6.4 \times 10^{-6}$	0.25	54		

Table 7. Area covered by non-buoyant or buoyant SNR bubbles. Case 1 assumes  $E_o = 0.5 \times 10^{51}$  ergs and  $B_{eff} = 2.5 \mu\text{G}$ . Case 2 assumes  $E_o = 0.5 \times 10^{51}$  ergs and  $B_{eff} = 5.0 \mu\text{G}$ . Case 3 assumes  $E_o = 1.0 \times 10^{51}$  ergs and  $B_{eff} = 5.0 \mu\text{G}$

Case	Coverage (%) (stationary)	Coverage (%) (drag coefficient = 1)	Coverage (%) (drag coefficient = 0)
1	61	65	87
2	29	29	32
3	54	55	67

### 3.3. The C<sup>+3</sup>, N<sup>+4</sup>, and O<sup>+5</sup> Predictions for the Population of SNRs

Here, we estimate the time and space averaged column densities of collisionally ionized O<sup>+5</sup>, N<sup>+4</sup>, and C<sup>+3</sup> ions along high latitude lines of sight due to the population of isolated extraplanar SNRs. The column density of an ion residing above a height of  $\mathcal{Z}$  is  $\int_{\mathcal{Z}}^{\infty} (\text{Rate}_{\text{SN}}(z) \times \int \int_0^R n_{\text{ion}}(r, t) 4\pi r^2 dr dt) dz$ . We replace the integrals with summations. For each slab, we integrate the supernova explosion rate with respect to  $z$  from the bottom to the top of the slab (see Table 6), and multiply by the O<sup>+5</sup>, N<sup>+4</sup>, and C<sup>+3</sup> contributions made by a SNR born within the slab (see Table 3 for stationary SNRs). When calculating the O<sup>+5</sup>, N<sup>+4</sup>, and C<sup>+3</sup> contributions made by buoyant SNRs, we take into account the extended lifetime of the SNR and the time spent in more rarefied environments. We then sum across all slabs above  $z = 130$  pc. Table 8 tabulates the resulting average column densities, for remnants that are assumed to be buoyant as well as those that are not. For example, the high latitude sky average O<sup>+5</sup> column density ranges from 2.3 to  $6.3 \times 10^{13} \text{ cm}^{-2}$ , depending on the simulation parameters and drag coefficient. This range may appear to be quite compact. Moderately buoyant SNRs would produce only 3 to 20% more O<sup>+5</sup> than stationary SNRs, while unfettered SNRs would produce 35 to 110% more O<sup>+5</sup> than stationary SNRs. For identical drag coefficients, Cases 1, 2, and 3 vary by a factor of 2.1 to 2.4, primarily due to the factor of 2 variation in assumed explosion energy. Interestingly, increasing the nonthermal pressure by a factor of 4 (from Case 1 to Case 2) slightly decreases the net O<sup>+5</sup> contribution. The reason for this phenomenon is that remnants experiencing greater nonthermal pressure are smaller, therefore denser, therefore more luminous, and therefore shorter lived. Note that Table 8’s values were found by averaging over many SNRs and even parts of the sky lacking SNRs. For predictions of O<sup>+5</sup>, N<sup>+4</sup>, and C<sup>+3</sup> column densities *within* individual SNRs, as a function of age and radius, see Paper I.

The height distribution of the O<sup>+5</sup>-rich gas in extraplanar SNRs is illustrated in Figure 2. For all choices of simulation parameters and drag coefficients, the  $z = 390$  to 670 pc slab makes the largest contribution to the sky averaged O<sup>+5</sup> column density. In Section 4.2, we will add the local O<sup>+5</sup> distribution and compare the result with *Copernicus*, *ORFEUS*, and *FUSE* observations.

Figure 3 displays the distribution of buoyant velocities for the population of supernova remnants. In making these plots, we assumed that the drag coefficient is 0 or 1. No plot is needed for the stationary SNRs, because their buoyant velocities are 0 km s<sup>-1</sup>. The plotted buoyant velocities are directed away from the Galactic plane. The first step in calculating the distributions was to calculate each remnant’s buoyant velocity as a function of time by integrating the buoyant acceleration with respect to time using small time steps. We assumed that buoyancy does not tear the remnants apart, so the calculated buoyant velocity

was assumed to pertain to the entire supernova remnant. Remnants born at different heights above the plane have different buoyancy histories. Thus, the final distributions of velocities were found by making weighted compilations of the remnants' buoyancy histories, where the weightings were proportional to the supernova explosion rate in the given slab. Case 1 ( $E_o = 1.0 \times 10^6$  ergs,  $B_{eff} = 5\mu\text{G}$ ) remnants are the most buoyant, probably because the small assumed ambient nonthermal pressure allows the hot bubbles to expand to greater volumes, lowering the internal density and raising their buoyancy. Case 2 remnants are the least buoyant for the converse reason. With drag coefficients of 0 and 1, we only see the  $\text{O}^{+5}$ -rich gas moving away from the plane; we do not see it stall and begin to fall back toward the plane. However, we saw the  $\text{O}^{+5}$ -rich gas rise and fall in preliminary estimates using larger drag coefficients. If there is moderate drag ( $C = 1$ ) then the typical buoyant velocity will hover around  $20 \text{ km sec}^{-1}$ . If there is no drag ( $C = 0$ ), then the typical buoyant velocity increases to  $\sim 70$  to  $\sim 100 \text{ km sec}^{-1}$ . If we were to observe such remnants, relative motions within the Galaxy would probably increase the spread of observed velocities, as would motion within the remnants themselves (see Paper I for estimates). Observations pointed at non-zenith directions record only the radial velocity, a trigonometric fraction of the velocity in the vertical direction.



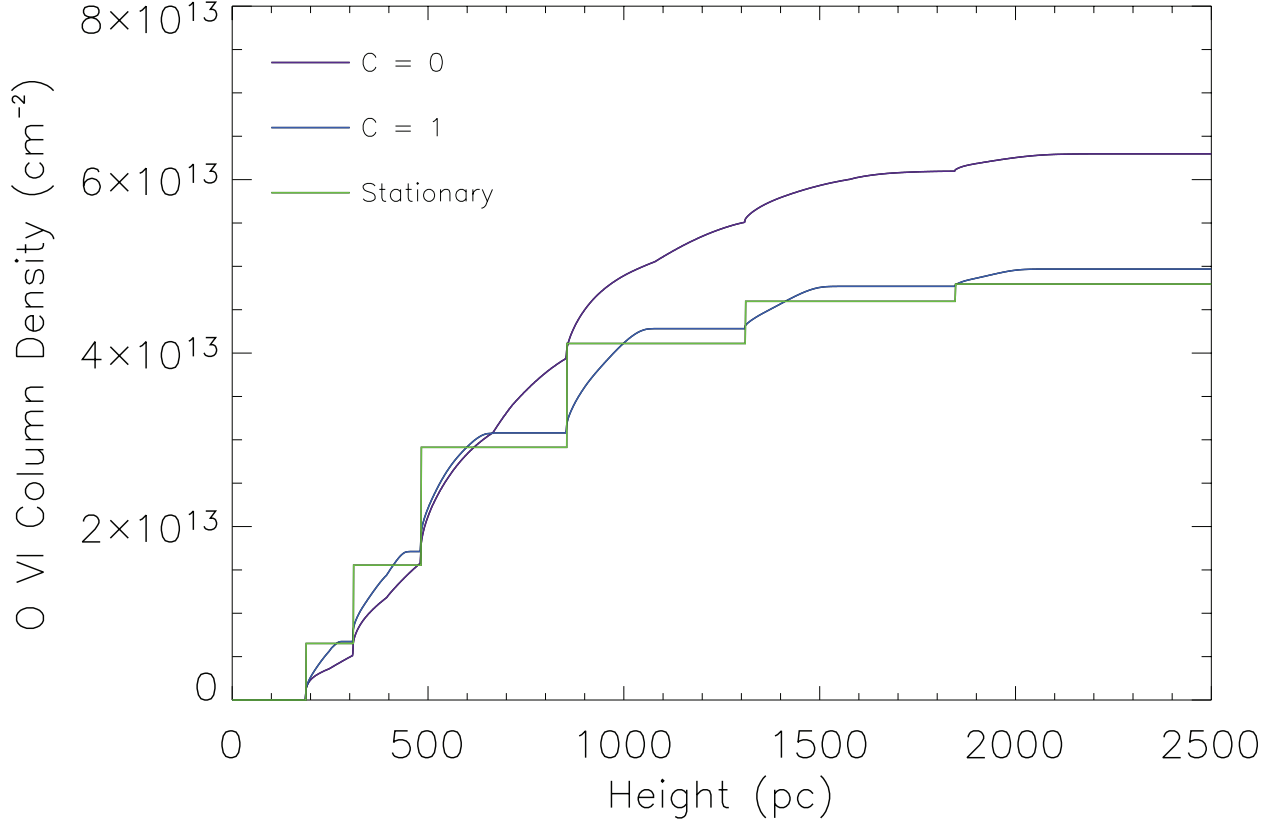


Fig. 2.— The  $O^{+5}$  column density expected to reside on vertical sightlines extending from the Earth to given heights above the plane, as a function of height above the plane. Various choices of buoyancy are marked by color. Green denotes a population of stationary SNRs. Blue denotes a population of moderately buoyant SNRs (drag coefficient = 1). Purple denotes a population of unrestrainedly buoyant SNRs (drag coefficient = 0). Independent of the choice of drag coefficient, the  $z = 390$  to  $670$  pc slab makes the greatest contribution to the total column density through the halo. Note that the  $O^{+5}$  *appears* to begin at  $z = 190$  pc, only because we set off the lowest SN explosions at the representative height for the lowest included slab, which is  $z_2 = 190$  pc. As in Figure 1, the simulated SNRs have an explosion energy of  $1.0 \times 10^{51}$  ergs and ambient effective magnetic field of  $5.0 \mu\text{G}$  (i.e. Case 3).

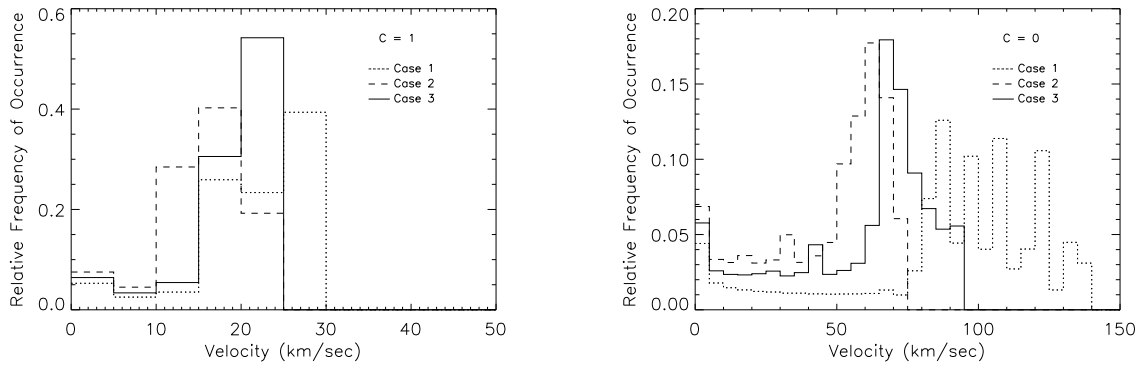


Fig. 3.— Distribution in buoyant velocity among the population of extraplanar supernova remnants, assuming moderate drag ( $C = 1$ , left figure) or no drag ( $C = 0$ , right figure). In addition to buoyant bulk velocity directed away from the Galactic plane, the young remnants will also exhibit expansion velocities. Detailed predictions of the expansion are provided in Paper I.

The procedure for calculating the high ion resonance line intensities is very similar to that for calculating the column densities. Theoretically, the average intensities are given by  $\int_{\mathcal{Z}}^{\infty} (\text{Rate}_{\text{SN}}(z) \times \int L(z, t) dt) dz / (4\pi \text{steradians})$ . We replace the integrals with summations. The resulting intensities are listed in Table 9. Allowing unrestrained buoyancy increases the sky-averaged intensities by only 20% or less, thus much less significantly than it affects the high-stage ion column densities. Buoyancy mostly affects the very late-term evolution of the remnants by extending their lives and elevating them into more rarefied surroundings. However, old remnants are dim and moving them to more rarefied surroundings makes them even dimmer. Therefore, these two influences on net photon production counteract each other. For the same reason, we see that buoyancy has almost no effect in the following calculations of 1/4 keV X-ray intensity.

Table 8. The model population of SNRs in the thick disk produce the following sky-averaged  $O^{+5}$ ,  $N^{+4}$ , and  $C^{+3}$  column densities. Case 1 assumes  $E_o = 0.5 \times 10^{51}$  ergs and  $B_{eff} = 2.5 \mu\text{G}$ . Case 2 assumes  $E_o = 0.5 \times 10^{51}$  ergs and  $B_{eff} = 5.0 \mu\text{G}$ . Case 3 assumes  $E_o = 1.0 \times 10^{51}$  ergs and  $B_{eff} = 5.0 \mu\text{G}$

Ion and Case	Column Density (ions $\text{cm}^{-2}$ ) (stationary SNR)	Column Density (ions $\text{cm}^{-2}$ ) (drag coefficient = 1)	Column Density (ions $\text{cm}^{-2}$ ) (drag coefficient = 0)
<u><math>O^{+5}</math></u>			
1	$2.5 \times 10^{13}$	$2.7 \times 10^{13}$	$4.0 \times 10^{13}$
2	$2.3 \times 10^{13}$	$2.4 \times 10^{13}$	$2.6 \times 10^{13}$
3	$4.8 \times 10^{13}$	$5.0 \times 10^{13}$	$6.3 \times 10^{13}$
<u><math>N^{+4}</math></u>			
1	$2.6 \times 10^{12}$	$2.9 \times 10^{12}$	$4.2 \times 10^{12}$
2	$1.7 \times 10^{12}$	$1.8 \times 10^{12}$	$2.1 \times 10^{12}$
3	$3.4 \times 10^{12}$	$3.5 \times 10^{12}$	$4.7 \times 10^{12}$
<u><math>C^{+3}</math></u>			
1	$5.3 \times 10^{12}$	$6.3 \times 10^{12}$	$1.1 \times 10^{13}$
2	$3.7 \times 10^{12}$	$3.8 \times 10^{12}$	$5.0 \times 10^{12}$
3	$7.0 \times 10^{12}$	$7.4 \times 10^{12}$	$1.2 \times 10^{13}$

Table 9. The model population of SNRs in the thick disk produce the following sky-averaged  $O^{+5}$ ,  $N^{+4}$ , and  $C^{+3}$  resonance line doublet intensities. Case 1 assumes  $E_o = 0.5 \times 10^{51}$  ergs and  $B_{eff} = 2.5 \mu\text{G}$ . Case 2 assumes  $E_o = 0.5 \times 10^{51}$  ergs and  $B_{eff} = 5.0 \mu\text{G}$ . Case 3 assumes  $E_o = 1.0 \times 10^{51}$  ergs and  $B_{eff} = 5.0 \mu\text{G}$

Ion and Case	Intensity (photon $\text{s}^{-1} \text{cm}^{-2} \text{sr}^{-1}$ ) (stationary SNR)	Intensity (photon $\text{s}^{-1} \text{cm}^{-2} \text{sr}^{-1}$ ) (drag coefficient = 1)	Intensity (photon $\text{s}^{-1} \text{cm}^{-2} \text{sr}^{-1}$ ) (drag coefficient = 0)
<u><math>O^{+5}</math></u>			
1	840	850	920
2	940	960	1000
3	1800	1900	2100
<u><math>N^{+4}</math></u>			
1	130	140	150
2	130	130	140
3	240	250	270
<u><math>C^{+3}</math></u>			
1	390	390	410
2	370	370	380
3	780	790	830

### 3.4. The X-ray Predictions for the Population of SNRs

Following the procedures outlined in the previous two subsections, we estimate the average  $\frac{1}{4}$  keV surface brightness due to the ensemble of extraplanar supernova remnants (see Table 10). The average  $\frac{1}{4}$  keV countrate is  $120$  to  $320 \times 10^{-6}$  counts  $\text{s}^{-1}$   $\text{arcmin}^{-2}$ , depending on the choice of explosion energy, magnetic pressure, and to a minute extent, drag coefficient. These estimates would increase by about 50% if we were to add the  $z_1$  SNRs between  $z = 21$  and  $130$  pc. The predictions are insensitive to buoyancy for the same reason as the high ion intensities are little affected by buoyancy - the longer lifetimes of buoyant remnants are counteracted by their lesser luminosities in old age.

Because we have averaged the SNR populations' brightness over the entire high latitude sky, the resulting average countrate is less than the countrate from individual remnants, especially young remnants. Roughly half of the soft X-rays are emitted during the bright, but brief stage before the remnant forms a cool shell. The remaining half are emitted later, when the old, dim remnants are difficult to identify. Observationally, the collective emission from unidentifiable remnants covering half of the sky would be construed as an X-ray background, punctuated by a few bright arcs tracing the limbs of young remnants. We expand on this description in the following subsection.

Table 10. Sky-Averaged 1/4 keV Countrates (in the ROSAT R1 + R2 bands) from the Population of SNRs above  $z = 130$  pc. Case 1 assumes  $E_o = 0.5 \times 10^{51}$  ergs and  $B_{eff} = 2.5 \mu\text{G}$ . Case 2 assumes  $E_o = 0.5 \times 10^{51}$  ergs and  $B_{eff} = 5.0 \mu\text{G}$ . Case 3 assumes  $E_o = 1.0 \times 10^{51}$  ergs and  $B_{eff} = 5.0 \mu\text{G}$

Case	Countrate ( $10^{-6} \frac{\text{counts}}{\text{s arcmin}^2}$ ) (stationary SNR)	Countrate ( $10^{-6} \frac{\text{counts}}{\text{s arcmin}^2}$ ) (drag coefficient = 1)	Countrate ( $10^{-6} \frac{\text{counts}}{\text{s arcmin}^2}$ ) (drag coefficient = 0)
1	120	120	120
2	130	130	130
3	310	310	320

### 3.5. Spatial Appearance

The high latitude sky (outside of superbubbles) should be comprised of three types of regions, those having bright young remnants seen in projection ( $\sim 0.2\%$  of sky), those having dimmer older remnants seen in projection ( $\sim 30$  to  $\sim 90\%$  of sky), and those having no remnants ( $\sim 10$  to  $\sim 70\%$  of sky). The young remnants should appear edge brightened in  $\frac{1}{4}$  keV X-ray emission,  $O^{+5}$ ,  $N^{+4}$ , and  $C^{+3}$  emission, and in numbers of  $O^{+5}$ ,  $N^{+4}$ , and  $C^{+3}$  ions. For example, the limb of a pre-shell formation remnant evolving in an  $n = 0.01 \text{ cm}^{-3}$  environment emits more than  $3000 \times 10^{-6} \frac{1}{4} \text{ keV counts s}^{-1} \text{ arcmin}^{-2}$ . It would be easily observed. Remnants evolving nearer to the plane (i.e. at  $z < 1300 \text{ pc}$ ) would be even brighter.

As the edge of its hot bubble cools below  $\sim 10^{5.7} \text{ K}$  a remnant loses its sharply edge-brightened look. It becomes slightly edge brightened and then centrally brightened (see Papers I and II for radial profiles of sample SNRs). Its total luminosity plummets. Our sample SNR's  $\frac{1}{4}$  keV surface brightness drops to  $< 500 \times 10^{-6} \text{ counts s}^{-1} \text{ arcmin}^{-2}$ . An old remnant should be difficult to recognize, considering that it may be outshone by the unobscured Local Bubble ( $\sim 300$  to  $\sim 800 \times 10^{-6} \text{ counts s}^{-1} \text{ arcmin}^{-2}$ ) combined with the extragalactic background ( $\sim 400 \times 10^{-6} \text{ counts s}^{-1} \text{ arcmin}^{-2}$ , de-absorbed). If an old remnant were to be detected in the X-ray regime, it should exhibit a soft spectrum and strong recombination edges (see Paper II for spectra of sample SNRs). Rather than being stars of the show, these remnants would create mottled soft X-ray and high stage ion backgrounds. Note that if  $O^{+5}$  column density and  $1/4$  keV maps were made from the SNR simulations, they would probably look somewhat dissimilar because of the significantly different time evolution in these observables.

## 4. Comparison between Simulations and Observations

### 4.1. Soft X-rays

Early, modest angular resolution surveys (the Wisconsin Rocket Program, McCammon *et al.* 1983, McCammon *et al.* (1983), SAS 3, Marshall & Clark (1984) and the HEAO 1 A-2 Low Energy Detectors, Garmire *et al.* (1992)) detected bright soft X-ray ( $\sim \frac{1}{4}$  keV) emission from every direction on the sky. The maps show considerable structure and identifiable features such as Loop I, the Eridanus Soft X-ray Enhancement, and the Monogem Ring. The poles are brighter than the equator and the northern polar region is brighter than the southern polar region. Most of the observed soft X-rays originate in the Local Bubble (a  $\sim 60 \text{ pc}$  radius region surrounding the sun) and the Milky Way's halo. Extragalactic sources



produce a fraction of the average observed total (McCammon et al. 1976; Snowden & Pietsch 1995). Small contributions to the flux observed at low latitudes are made by pre-radiative phase remnants and Galactic point sources. (Rosner et al. 1981).

The halo and extragalactic soft X-rays are attenuated by the layer of diffuse neutral gas in the disk, so that only  $\sim 2/3$ rds reach the solar system. In directions with especially opaque clouds, distinct “shadows” appear in the X-ray maps. It was by observing shadowed regions with the Röntgensatellit Position Sensitive Proportional Counter (or ROSAT PSPC), that researchers first conclusively demonstrated the emissivity of the distant (halo plus extragalactic) component (Snowden et al. 1991; Burrows & Mendenhall 1991; Kerp et al. 1993; Snowden et al. 1994; Wang & Ye 1996). More recently, Snowden et al. (1998, 2000); Kuntz & Snowden (2000) extended this type of analysis to the entire sky. Their estimates for the surface brightness of the de-absorbed distant component range from  $\sim 400$  to  $3000 \times 10^{-6}$  ROSAT 1/4 keV counts  $s^{-1}$  arcmin $^{-2}$ , depending on the direction. The high end of the quoted range is misleading, because it refers to the flux from anomalous objects, such as the Draco region, and intermediate distance objects, such as the North Polar Spur and the Eridion Superbubble, which the analysis technique partitioned between the near and far components. Due to the North Polar Spur and Draco, the map of the northern sky is brighter and more complex than that of the southern sky. The southern sky provides only  $\sim 400$  to  $1000 \times 10^{-6}$  counts  $s^{-1}$  arcmin $^{-2}$ , (unabsorbed) and has an average count rate for  $b < -65^\circ$  of  $810 \times 10^{-6}$  counts  $s^{-1}$  arcmin $^{-2}$ . Because the southern halo is far less “polluted” by anomalous regions, this paper takes it as the standard. Next, the extragalactic component must be subtracted from the distant component to yield the halo flux. From shadowing studies of nearby spiral galaxies, the 1/4 keV extragalactic intensity has been estimated to be about  $30 \text{ keV cm}^{-2} \text{ s}^{-1} \text{ sr}^{-1} \text{ keV}^{-1}$ , equivalent to  $400 \times 10^{-6}$  counts  $s^{-1}$  arcmin $^{-2}$  in the *ROSAT*  $\frac{1}{4}$  keV band (see Snowden & Pietsch (1995); Barber et al. (1996); Cui et al. (1996)). The extragalactic surface brightness should be fairly smooth and isotropic. Subtracting its flux leaves only  $\sim 400 \times 10^{-6}$  counts  $s^{-1}$  arcmin $^{-2}$  (unabsorbed), which is attributable to the Milky Way’s southern halo.

In comparison with our simulation results,  $310 \times 10^{-6}$  counts  $s^{-1}$  arcmin $^{-2}$ , or  $3/4$  of the observed emission could come from the population of extraplanar SNRs if their explosion energies are  $1 \times 10^{51}$  ergs, their surrounding effective magnetic field is  $5 \mu\text{G}$ , and they are stationary. Our estimate rises to  $400 \times 10^{-6}$  counts  $s^{-1}$  arcmin $^{-2}$ , or 100% of the observationally determined surface brightness if we use McKee & Williams (1997)’s isolated massive progenitor SN rate rather than averaging it with Ferrière (1998)’s rate. Assuming the more modest rate and the full range of explored parameters yields estimated brightnesses of 120 to  $320 \times 10^{-6}$  counts  $s^{-1}$  arcmin $^{-2}$ , or 30% to 80% of the observationally determined flux.

Other important characteristics of the X-ray emitting gas include its vertical extent, degree of spatial non-uniformity, and temperature. Determining the height of the X-ray emitting plasma is difficult, but shadowing by low, intermediate, and high velocity clouds provides some indication. After comparing the 1/4 keV X-ray emission with the H I column densities in and around the M complex, Herbstmeier et al. (1995) concluding that nearly all of the distant emission originates beyond the low velocity clouds ( $z_{cloud} \lesssim 200$  pc), while some originates below and some originates beyond the high velocity clouds ( $1.5 \text{ kpc} \lesssim z_{cloud} \lesssim 4.4 \text{ kpc}$ ). Hence the distribution of extraplanar SNRs is in rough agreement with the distribution of X-ray emitting gas.

The eye can easily identify patchiness in the 1/4 keV survey maps of Snowden et al. (1998). Quantitatively, the halo emission varies by a factor of 2 over angular scales of  $\sim 20^\circ$  (Snowden et al. 1997). On a smaller scale, Burrows & Mendenhall (1991) found that the emission behind the Draco cloud varies by 1/3 from the northern to the southern half of the region ( $\sim 1^\circ$ ). In the Milky Way’s south, the flux is arranged in a fringe of bright regions northward of  $b \sim -45^\circ$  (which may be artifacts of the deabsorption analysis), a mottled background, and a couple of noticeably bright regions below  $l \sim -45^\circ$  (i.e. the regions around  $l = 247^\circ, b = -64^\circ$  and  $l = 215^\circ, b = -68^\circ$ ). We think that these two bright regions must be emitting features rather than artifacts of the analysis technique because there is no significant spatial correlation between the distant emission map and the absorption map used in Snowden et al. (1997)’s analysis. The shapes of these bright features can be better seen in the less smoothed total observed surface brightness map of Snowden et al. (1997). This map shows that the larger feature, the one around  $l = 247^\circ, b = -64^\circ$  has a fairly crisp outer edge and a crescent, edge brightened shape.

Approximately 1 bright, pre-shell formation phase SNRs is expected to reside in the halo of each hemisphere above  $b \sim |50^\circ|$  and  $z \sim 130$  pc. The feature around  $l = 247^\circ, b = -64^\circ$  is a reasonable candidate for a pre-shell formation phase halo SNR. The Dickey & Lockman (1990) H I survey shows a cloud abutting the thickest part of the larger crescent. We were unable to find additional confirmation in radio synchrotron surveys (Haslam et al. 1982; Alvarez et al. 97) or the *ROSAT* 3/4 keV soft X-ray survey (Snowden et al. 1997). The lack of confirmation is not a confirmation of the lack of a remnant for the following reasons. Caswell & Lerche (1979) empirically determined that, on average, the radio brightness of a SNR decreases with  $z$ . Correspondingly, our simulations of SNRs in low density environments found that their shells were not very dense and so probably not very emissive in synchrotron emission. In addition, the 3/4 keV emission from the simulated SNRs wanes far earlier than does the 1/4 keV emission, thus a remnant can be observed in 1/4 keV X-rays after it has become too dim to be observed in 3/4 keV X-rays. The smaller feature, which is around  $l = 215^\circ, b = -68^\circ$ , also has an edge brightened crescent shape, though it is less crisp and

less bright than the larger feature. Suggesting that this is a SNR would be more speculative.

The next element of study is the mottled background. Galactic X-ray emitting gas covers roughly half of sky above  $|b| = 45^\circ$  sky in Snowden et al. (1998)'s 1/4 keV survey map (assuming that the extragalactic sources contribute  $400 \times 10^{-6}$  counts  $\text{s}^{-1}$   $\text{arcmin}^{-2}$ ). This compares well with the fraction of the sky covered by post shell formation phase SNRs (30 to 90%).

Finally, we turn to the spectral temperature of the emission. Several studies of *ROSAT*'s low resolution spectra, including Kuntz & Snowden (2000)'s and Snowden et al. (2000)'s found that the high latitude extraplanar emission has two temperature components, a  $\sim 10^6$  K, non-homogeneously distributed component and a weaker,  $\sim 3 \times 10^6$  K, homogeneously distributed component. Because they are distributed differently, the  $10^6$  K and the  $3 \times 10^6$  K components are thought to originate in different regions. If extraplanar SNRs are producing much of the  $10^6$  K component, then we would expect their soft X-ray emission to look like a  $10^6$  K spectrum. This was found to be the case when the simulated spectra were treated as real spectra (i.e. convolved with the *ROSAT* response function and fit to collisional equilibrium spectral models), in Paper II. Note that the SNR plasma was often out of collisional ionizational equilibrium and as a result, the gas's temperature was generally higher or lower than the temperature calculated from its spectrum.

## 4.2. $\text{O}^{+5}$ Column Densities and Intensities

Soft X-rays are emitted by plasma whose carbon, nitrogen, and oxygen atoms have been ionized to the hydrogen-like and helium-like levels. The neighboring ions, lithium-like ions of carbon, nitrogen, and oxygen can be observed by absorption or emission in their strong resonance line doublets in the ultraviolet region of the electromagnetic spectrum ( $\text{O}^{+5}$ : 1032, 1038 Å;  $\text{N}^{+4}$ : 1239, 1243 Å;  $\text{C}^{+3}$ : 1548, 1551 Å). Owing to its large ionization potential, the observed  $\text{O}^{+5}$  is thought to be produced via collisional ionization.  $\text{N}^{+4}$ , and  $\text{C}^{+3}$  can be produced via photoionization or collisional ionization. In fact, Slavin et al. (2000) have already shown that substantial numbers of extraplanar  $\text{C}^{+2}$  ions have been ionized to  $\text{C}^{+3}$  by SNR photons. Our code simulates collisional ionization and recombination but does not simulation photoionization. Therefore we will confine our comparisons to the soft X-ray and  $\text{O}^{+5}$  data.

Hundreds of Milky Way sightlines have been surveyed for  $\text{O}^{+5}$  absorption (Jenkins & Meloy (1974); Jenkins (1978a); Hurwitz & Bowyer (1996); Widmann et al. (1998); Zsargó et al. (2003); Wakker et al. (2003); Oegerle et al. (2005)). The data suggest that this

ion is distributed inhomogeneously and is more plentiful nearer to the plane than at greater distances. The column density vs height data are plotted in the standard fashion in Figure 4. For comparison, our most productive model ( $E_o = 1.0 \times 10^{51}$  ergs,  $B_{eff} = 5\mu\text{G}$ , drag coefficient = 0) and least productive model ( $E_o = 0.5 \times 10^{51}$  ergs,  $B_{eff} = 5\mu\text{G}$ , nonbuoyant) have been plotted. Because our models begin at  $z = 130$  pc, we have also plotted the expected local contribution (taken from Oegerle et al. (2005)) and added it to our models in order to obtain the total quantity of  $\text{O}^{+5}$  ions expected to reside between the Sun and various heights above the plane. The extraplanar SNR column densities reasonably track the observations within the relevant height range ( $\sim 130 \leq z \leq \sim 2000$  pc). Thus, extraplanar SNRs can explain both the observed column densities and the increase in column density with height, within this  $z$  range.

The extraplanar SNR model was not meant to explain the  $\text{O}^{+5}$  observed within the first hundred or so parsecs of the Sun. That material has been attributed to the Local Bubble and clouds within it. Nor does the model explain the  $\text{O}^{+5}$  residing beyond  $z \sim 2000$  pc (about 6 times the SN scaleheight). That column density requires another source.

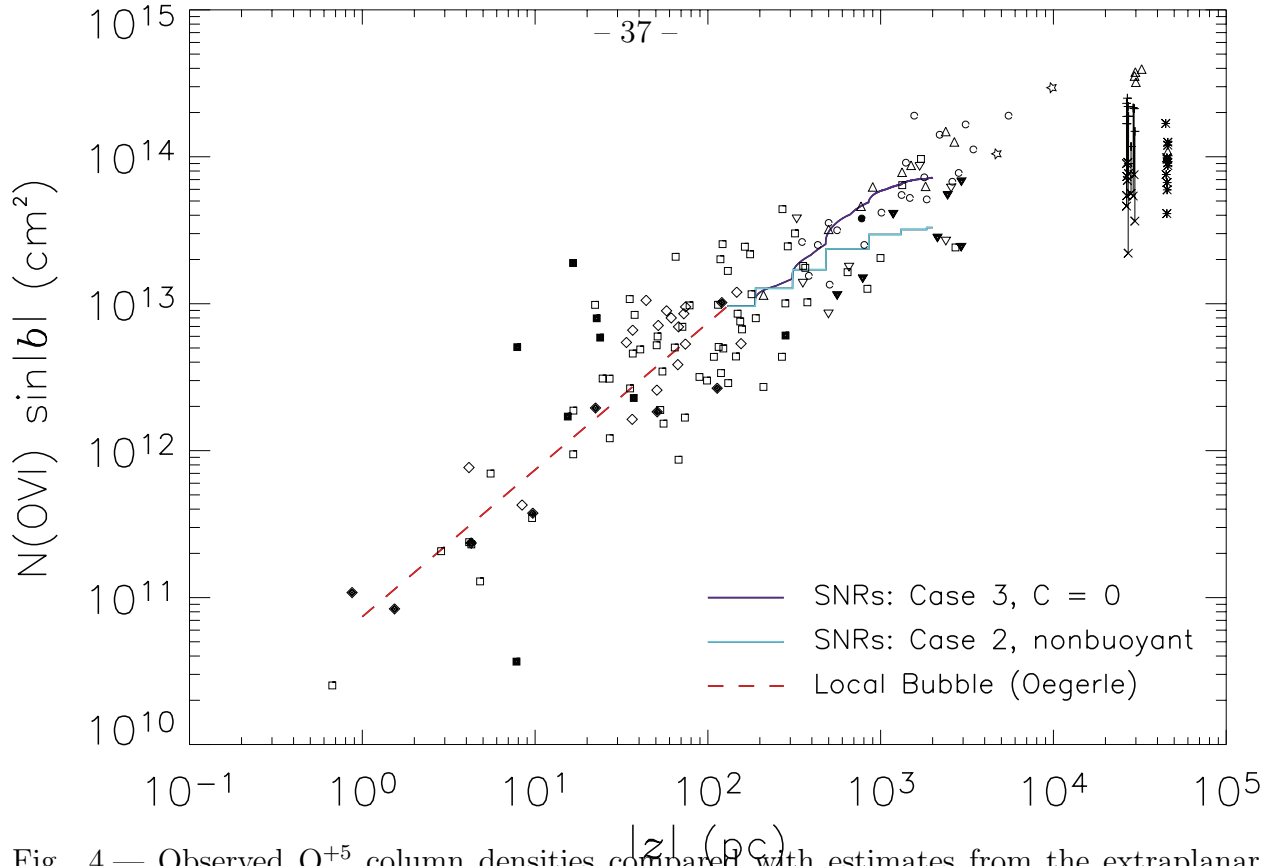


Fig. 4.— Observed  $O^{+5}$  column densities compared with estimates from the extraplanar SNR simulations (blue and purple curves) combined with the estimated Local Bubble contribution (Oegerle et al. (2005), dashed red line). The purple and blue curves correspond to the least and most prolific extraplanar SNR models, respectively. The squares mark Jenkins (1978a)’s *Copernicus* observations. The *ORFEUS* observations by Hurwitz & Bowyer (1996) are marked with downward pointing triangles while the *ORFEUS II* observations by Widmann et al. (1998) are marked with upward pointing triangles. The *FUSE* Local Bubble observations by Oegerle et al. (2005) are marked with diamonds. The *FUSE* Milky Way halo observations by Zsargó et al. (2003) are marked with circles. The two *FUSE* Milky Way star observations by Wakker et al. (2003) are marked with stars. For the above plotting, detections are marked with open symbols and upper limits are marked by solid symbols. The Howk et al. (2002) SMC observations are marked with asterisks. The Howk et al. (2002) LMC observations of  $O^{+5}$  within the velocity range  $v \leq \pm 50 \text{ km s}^{-1}$  are plotted with Xs. These column densities plus higher positive velocity  $O^{+5}$  observed along the same sightlines are plotted with pluses. All of the Howk et al. (2002) observations were detections. Vertical lines connect the higher and lower LMC datapoints. The agreement between the model and the data suggests that the extraplanar supernova remnants reasonably explain the  $O^{+5}$  observed between  $z \sim 130 \text{ pc}$  and  $z \sim 2000 \text{ pc}$ .

The upper limits and weak detections in Figure 4 demonstrate that the  $O^{+5}$ -rich gas does not completely cover the high latitude, extraplanar sky. Of the sightlines terminating above 130 pc, 1/8 have  $O^{+5}$  upper limits and an additional 1/8 have such small column densities (less  $O^{+5}$  than expected from local material) that we can assume they have not encountered extraplanar  $O^{+5}$ . In comparison, our simulation results also imply incomplete (30 to 90%) sky coverage.

Wakker et al. (2003)'s Figure 9 displays the column density vs velocity distribution of the  $O^{+5}$  features observed in their survey. The distribution consists of a cluster of features with  $-50 \text{ km sec}^{-1} \leq v \leq 50 \text{ km sec}^{-1}$  plus separate clusters having  $-400 \text{ km sec}^{-1} \leq v \leq -100 \text{ km sec}^{-1}$  and  $75 \text{ km sec}^{-1} \leq v \leq 400 \text{ km sec}^{-1}$ . The high velocity clusters are not symmetric; the positive high velocity cluster extends to lower speeds and column densities than does the negative high velocity cluster. In comparing with our simulation results, we must keep in mind that our predicted velocities are in the vertical direction while Wakker et al. (2003)'s velocities are along high latitude lines of sight. Thus, we would want to multiply the observed velocities by cosecant(latitude), where the typical latitude is around  $50^\circ$  to  $60^\circ$ . In our calculations, the greatest velocity to which the extraplanar SNRs are accelerated is  $140 \text{ km sec}^{-1}$  and this is for only one set of parameter choices. Such remnants would contribute to the moderate speed, low column density portion of the observed  $75 \text{ km sec}^{-1} \leq v \leq 400 \text{ km sec}^{-1}$  cluster, though they would not produce the entire cluster or its negative velocity counterpart. If extraplanar SNRs experience moderate to large drag, then their  $O^{+5}$  features would contribute to the  $-50 \text{ km sec}^{-1} \leq v \leq 50 \text{ km sec}^{-1}$  cluster. While both scenarios lie within the broad range of possibility, the first scenario is highly constrained and thus unlikely. It is far more likely that the observed nearly symmetrical, low velocity distribution includes extraplanar SNRs who have experienced moderate to large drag.

Now we turn to  $O^{+5}$  resonance line emission. Observations of the resonance line intensity have the potential to nicely complement the column density data. The intensity produced by a column of  $O^{+5}$  ions is sensitive to the local volume density and temperature. Emissivity goes as density squared. Hot gas emits readily, while warm/hot gas emits sparingly and cool gas does not emit. Using *Voyager*, Murthy et al. (2001) set upper limits on the  $O^{+5}$  doublet intensity for hundreds of sightlines. Their tightest was a 90% confidence upper limit of  $2600 \text{ photons s}^{-1} \text{ cm}^{-2} \text{ sr}^{-1}$  toward  $\ell = 117^\circ, b = 51^\circ$ . Using *FUSE*, Shelton et al. (2001), Dixon, et al. (2001), Shelton (2002), and Otte et al. (2003) have detected  $O^{+5}$  emission from a handful of high latitude directions outside of young SNRs and superbubbles. Their doublet intensities range from  $\sim 2400$  to  $\sim 4700 \text{ photons s}^{-1} \text{ cm}^{-2} \text{ sr}^{-1}$ . Ignoring the effects of absorption and subtracting the Local Bubble contribution ( $2\sigma$  upper limit =  $800 \text{ photons s}^{-1} \text{ cm}^{-2} \text{ sr}^{-1}$ , Shelton (2003)) leaves  $1600$  to  $4700 \text{ photons s}^{-1} \text{ cm}^{-2} \text{ sr}^{-1}$  to be attributed to the extraplanar sky. In comparison, our model predicts  $840$  to  $2100 \text{ photons s}^{-1} \text{ cm}^{-2}$

$\text{sr}^{-1}$ , with the variation mostly due to assumed explosion energy. Given that the extraplanar SNRs could explain the  $\text{O}^{+5}$  column density between  $z = 130\text{pc}$  and  $2000\text{ pc}$ , but not the higher  $\text{O}^{+5}$ , the same could be true of the emission. To determine the answer, we will need to know the typical height of the observed  $\text{O}^{+5}$  emission.

## 5. Summary

- This paper refines Papers I and II’s preliminary calculations of isolated extraplanar SNRs by modeling the decrease in interstellar density with height above the Galactic plane, considering buoyancy, exploring a wider range of explosion energies and nonthermal pressures and predicting a wider range of observables ( $\text{O}^{+5}$ ,  $\text{N}^{+4}$ ,  $\text{C}^{+3}$  emission and absorption column densities,  $1/4\text{ keV}$  X-ray surface brightness, area coverage, volume occupation, vertical velocity, and variation with height above the Galactic plane).
- The predicted average  $\text{O}^{+5}$  column density matches the observed distribution of column densities as a function of height above the Galactic plane. All 9 of our models (3 sets of explosion energies and ambient effective magnetic field strengths and 3 sets of drag coefficients) fell within the scatter in the observed  $N(\text{O}^{+5}) \sin |b|$  versus  $|z|$  for the height range of interest ( $z$  up to 6 times the SN scaleheight). See Subsection 4.2.
- Isolated extraplanar SNRs can explain the Galactic halo’s  $1/4\text{ keV}$  X-ray brightness, within the precision of the SN rate estimates. Assuming that these SNRs explode with energies of  $1 \times 10^{51}$  ergs and experience an ambient effective magnetic field of  $5\ \mu\text{G}$ , then the population of isolated SNRs born above the Galactic H I layer (scaleheight  $\sim 130\text{ pc}$ ) produces a time and space averaged  $1/4\text{ keV}$  soft X-ray surface brightness of  $\sim 310 \times 10^{-6}\text{ ROSAT counts s}^{-1}\text{ arcmin}^{-2}$ . This is 80% of the observationally determined surface brightness of the Galaxy’s southern high latitude sky beyond the H I layer ( $400 \times 10^{-6}\text{ ROSAT counts s}^{-1}\text{ arcmin}^{-2}$ ). If we were to use a larger SN explosion rate, such as that estimated by McKee & Williams (1997), then the prediction would rise to  $400 \times 10^{-6}\text{ ROSAT counts s}^{-1}\text{ arcmin}^{-2}$ , accounting for the entire observationally determined surface brightness. However, using the rate adopted in this paper and the other choices of SN parameters yields average surface brightnesses as low as  $120 \times 10^{-6}\text{ ROSAT counts s}^{-1}\text{ arcmin}^{-2}$ . Buoyancy makes little difference here. See Subsection 4.1.
- The predicted average  $\text{O}^{+5}$  intensity ( $840$  to  $2100\text{ photons s}^{-1}\text{ cm}^{-2}\text{ sr}^{-1}$ ) contributes significantly to the observationally determined intensity originating beyond the Local Bubble ( $\sim 2400$  to  $\sim 4700\text{ photons s}^{-1}\text{ cm}^{-2}\text{ sr}^{-1}$ ). See Subsection 4.2.

- Before SNRs develop a cool shell, they are bright in 1/4 keV emission, and  $O^{+5}$ ,  $N^{+4}$ , and  $C^{+3}$  resonance line emission, and are rich in  $O^{+5}$ ,  $N^{+4}$ , and  $C^{+3}$  ions. After the shell forms, the remnants dim, but still harbor large numbers of lithium-like ions. Thus, the spatial distributions of 1/4 keV emission and  $O^{+5}$  column densities should be de-correlated, as found by observers (ex: Savage et al. (2003)'s, Figure 9).
- Old SNRs, which glow dimly in 1/4 keV X-ray and UV resonance line photons and retain observable numbers of lithium-like ions, should cover 30 to 90% of the high latitude sky. Young remnants, which glow brightly in these regimes should cover less than a percent of the high latitude sky. Correspondingly, maps of the observed soft X-ray background beyond the Galactic H I layer, outside of superbubbles, and after subtracting the extragalactic component appear mottled, as if roughly half the high latitude sky is covered with dim emitting regions while the other half is bare. The  $O^{+5}$  column density surveys also find null detections and low detections. See Subsections 3.5, 4.1, and 4.2.
- The fraction of volume occupied by hot supernova remnant bubbles peaks around the supernova scaleheight and is less than 10% at all heights. The volume filled by young remnants is only a fraction of a percent. See subsection 3.2.
- We calculated the vertical displacement and velocity distribution, assuming buoyant acceleration and zero to moderate drag. In the extreme case of unfettered buoyancy, the velocity can reach  $+140 \text{ km sec}^{-1}$ , but if SNRs experience modest drag, then their velocities will range from 0 to 30 km/sec. In order for the gas to rise and fall again, the drag coefficient must exceed 1.0. Buoyancy is not absolutely necessary to explain the observed vertical distribution of  $O^{+5}$  ions. See Figure 1 and Section 3.3.
- Of the explored range of parameters, we prefer Case 3 ( $E_o = 1.0 \times 10^{51}$  ergs,  $B_{eff} = 5.0\mu\text{G}$ ) because its predictions best match the high ion and soft X-ray data. The predictions from the other cases are factors of  $\sim 2$  to  $\sim 3$  lower. Of the explored range of drag coefficients, we prefer moderate to large drag, because it limits the buoyant velocity to  $50 \text{ km sec}^{-1}$  or less. High latitude observations find many  $O^{+5}$  features in this velocity range.
- This picture can be tested by: 1.) examining the high latitude crescent shaped bright X-ray regions ( $l \sim 247^\circ$ ,  $b \sim -64^\circ$  and  $l \sim 215^\circ$ ,  $b \sim -68^\circ$ ) to determine if they are the limbs of young remnants (see Subsection 4.1), and 2.) and testing the spectral features of the mottled dim 1/4 keV background for signatures of old, cooling, recombining SNR gas. (See Paper II.)



Acknowledgments:

The author would like to thank Don Cox, K.D. Kuntz, Loris Magnani, J. Scott Shaw, and Steve Lewis for their contributions to helpful discussions about the interstellar medium, observations, and buoyancy. This work was supported under NASA grant NNG04GD78G.

## REFERENCES

- Alvarez, H., Aparici, J., May, J., & Olmos, F., 1997, *A&AS*, 124, 315
- de Avillez, M. A., & Mac Low, M.-M. 2001, *ApJ*, 551, L57
- Barber, C. R., Roberts, T. P., & Warwick, R. S., 1996, *MNRAS*, 282, 157
- Benjamin, R. A., & Danly, L. 1997, *ApJ*, 481, 764
- Burrows, D. N., & Mendenhall, J. A., 1991, *Science*, 351, 629
- Caswell, J. L., & Lerche, I., 1979, *MNRAS*, 187, 201
- Cioffi, D. F. 1991, in *International Astronomical Union Symposium Proceedings Num. 144, The Disk-halo connection In Galaxies*, ed. H. Bloemen (the Netherlands), 355
- Cox, D. P., Shelton, R. L., Maciejewski, W., Smith, R. K., Plewa, T. Pawl, A., & Rozyczka, Michal, 1999, *ApJ*, 524, 179
- Cui, W. & Cox, D. P., 1992, *ApJ*, 401, 206
- Cui, W., Sanders, W. T., McCammon, D., Snowden, S. L., & Womble, D. S., 1996, *ApJ*, 468, 117
- Dickey, J. M., & Lockman, F. J., 1990, *ARA&A*, 28, 215
- Dixon, W. V., Sallmen, S., Hurwitz, M., & Lieu, R. 2001, *ApJ*, 552, L69
- English, J., Taylor, A. R., Mashchenko, S. Y., Irwin, J. A., Basu, S., & Johnstone, D. 2000, *ApJL*, 533, L25
- Ferrière, K. 1998, *ApJ*, 503, 700
- Ferrière, K. 1998, *ApJ*, 503, 759
- Ferrière, K. & Zweibel, E. G., 1991, *ApJ*, 383, 602
- Garmire, G. P., Nousek, J. A., Apparao, K. M. V., Burrows, D. N., Fink, R. L., & Kraft, R. P., 1992, 399, 694
- Grevesse, N., & Anders, E. 1989, in *AIP Conference Proceedings 183, Cosmic Abundances of Matter*, ed. C. J. Waddington, p. 1
- Haslam, C. G. T., Salter, C. J., Stoffel, H., & Wilson, W. E., 1982, *A&AS*, 47, 1

- Herbstmeier, U., Mebold, U., Snowden, S. L., Hartmann, D., Butler Burton, W., Moritz, P., Kalberla, P. M. W., & Egger, R., 1995, *A & A*, 298, 606
- Howk, J. C., Savage, B. D., Sembach, K. R., & Hoopes, C. G. 2002, *ApJ*, 572, 264
- Hurwitz, M., & Bowyer, S. 1996, *ApJ*, 465, 296
- Jenkins, E. B. 1978, *ApJ*, 219, 845
- Jenkins, E. B. 1978, *ApJ*, 220, 107
- Jenkins, E. B., & Meloy, D. A. 1974, *ApJ*, 193, 121
- Jones, E. M. 1973, *ApJ*, 182, 559
- Jones, T. W., Ryu, D., & Tregillis, I. L. 1996, *ApJ*, 473, 365
- Kerp, J., Herbstmeier, U., & Mebold, U. 1993, *A & A*, 268, L21
- Kuntz, K. D., & Snowden, S. L. 2000, *ApJ*, 543, 195
- Laming, J. M., Raymond, J. C., McLaughlin, B. M., & Blair, W. P. 1996, *ApJ*472, 267L
- Leahy, D. A., Nousek, J., & Hamilton, A. J. S. 1991, *ApJ*374, 218L
- Marshall, F. J., & Clark, G. W., 1984, *ApJ*, 287, 633
- McCammon, D., Meyer, S. S., Sanders, W. T., & Williamson, F. O., 1976, *ApJ*, 209, 46
- McCammon, D., Burrows, D. N., Sanders, W. T., & Kraushaar, W. L., 1983, *ApJ*, 269, 107
- McKee, C. F., & Williams, J. P., 1997, *ApJ*, 476, 144
- Murthy, J., Henry, R. C., Shelton, R. L., & Holberg, J. B. 2001, *ApJ*, 557, 47L
- Oegerle, W. R., Jenkins, E. B., Shelton, R. L., Bowen, D. V., & Chayer, P. 2005, *ApJ*, 622, 377
- Otte, B., Dixon, W. V., & Sankrit, R. 2003, *ApJ*, 586, 530
- Rosner, R., Avni, Y., Bookbinder, J., Giacconi, R., Golub, L., Harnden, F. R., Jr., Maxson, C. W., Topka, K., & Vaiana, G. S. 1981, *ApJL*, 249, L5
- Savage, B. D., et al., 2003, *ApJS*, 146, 125
- Shelton, R. L. 1998, *ApJ*, 504, 785

- Shelton, R. L. 1999, *ApJ*, 521, 217
- Shelton, R. L., Cox, D. P., Maciejewski, W., Smith, R. K., Plewa, T. Pawl, A., & Rozyczka, Michal, 1999, *ApJ*, 524, 179
- Shelton, R. L. et al. 2001, *ApJ*, 560, 730
- Shelton, R. L. 2002, *ApJ*, 569, 758
- Shelton, R. L. 2003, *ApJ*, 589, 261
- Shelton, R. L., Kuntz, K. D., & Petre, R., 2004, *ApJ*, 615, 275
- Slavin, J. D., & Cox, D. P. 1992, *ApJ*, 392, 131
- Slavin, J. D., & Cox, D. P. 1993, *ApJ*, 417, 187
- Slavin, J. D., McKee, C. F., & Hollenbach, D. J. 2000, *ApJ*, 541, 218
- Snowden, S. L., Mebold, U., Hirth, W., Herbstmeier, U., & Schmitt, J. H. M. M, 1991, *Science*, 252, 1529
- Snowden, S. L., McCammon, D., Burrows, D. N., & Mendenhall, J. A., 1994, *ApJ*, 424, 714
- Snowden, S. L., & Pietsch, W., 1995, *ApJ*, 452, 627
- Snowden, S. L., Egger, R., Freyberg, M. J., McCammon, D., Plucinsky, P. P., 1998, Sanders, W. T., Schmitt, J. H. M. M., Trümper, & J., Voges, 1997, *ApJ*, 485, 125
- Snowden, S. L., Egger, R., Finkbeiner, D., Freyberg, M. J., & Plucinsky, P. P., 1998, *ApJ*, 493, 715
- Snowden, S. L., Freyberg, M. J., Kuntz, K. D., & Sanders, W. T., 2000, *ApJ*, *ApJS*, 128, 171
- Wakker, B. P. et al., 2003, *ApJS*, 146, 1
- Wang, Q. D., & Ye, T., 1996, *New Astronomy*, 1, 245
- Widmann, H., et al. 1998, *A & A*, 338, L1
- Wolfire, M. G., McKee, C. F., Hollenbach, D., & Tielens, A. G. G. M, *ApJ*, 453, 673
- Zsargó, J., Sembach, K. R., Howk, J. C., & Savage, B. D. 2003, *ApJ*, 586, 1019